https://doi.org/10.5194/egusphere-2026-5457
Preprint. Discussion started: 2 November 2026
© Author(s) 2026. CC BY 4.0 License.

Radiative Transfer Modelling of Ka-band Microwave Interactions with Snow-Covered Freshwater Ice: Implications for SWOT KaRIn Property Retrieval

Peilin Chen[1], Grant Gunn[1], Julien Meloche[2]
[1] Department of Geography and Environmental Management, University of Waterloo, Waterloo, N2L 3G1, Canada
[2] Earth Systems Research and Integration Division, Environment Climate Change Canada, Canada

Correspondence to: Peilin Chen (peilin.chen1@uwaterloo.ca)

Abstract. Snow cover on lake ice plays an important role in regulating lake ice thermodynamics, making its characterization essential for understanding lake climatology and cryospheric processes. However, remote sensing studies of snow-covered lake ice remain limited, and the physical understanding of high-frequency radar backscatter from the coupled snow–ice system remains unclear. This study investigates the interactions between Surface Water and Ocean Topography (SWOT) Ka-band Radar Interferometer (KaRIn) observations and snow-covered lake ice by examining how snow and ice properties, together with radar acquisition geometry, influence the relative contributions of different scattering mechanisms. A field campaign was conducted on Kluane Lake, Yukon, during the winter season of 2026, where in-situ snow and ice properties were measured coincident with eight SWOT acquisitions from five orbital passes. The Snow Microwave Radiative Transfer (SMRT) model was used to simulate Ka-band backscatter and perform sensitivity analyses of snow/ice properties and sensor configurations. A second-order iterative scattering solver was implemented to quantify backscatter contributions from individual snow and ice layers and to investigate the evolution of the dominant scattering mechanism. Modelled and observed backscatter showed good agreement, with RMSEs of 1.14 dB using smooth snow configurations and 1.08 dB for using rough snow configurations and Pearson correlation coefficients of approximately 0.95 at both configurations. Results indicate that the ice surface generally dominates KaRIn backscatter over snow-covered lake ice, while the relative contributions of the snow surface and snow volume increase under specific combinations of incidence angle, snow depth, and snow microstructure. These findings demonstrate the importance of explicitly considering snow–ice interactions when interpreting Ka-band observations and provide a physical basis for developing snow and ice retrieval approaches from current and future Ka-band satellite missions.

1 Introduction

Seasonal snow cover fundamentally controls lake ice growth and thermodynamics by acting as an effective thermal insulator, ultimately influencing lake ice thickness and energy exchange (Brown and Duguay, 2010). Consequently, accurately characterizing snow water equivalent (SWE) over lake ice is essential for understanding lake ice processes, improving hydroclimatology studies, and is an essential input for lake ice thermodynamic models (Pouw et al., 2023). However, measuring SWE over lakes remains challenging (Gunn et al., 2021), partly because lake ice introduces additional

https://doi.org/10.5194/egusphere-2026-5457
Preprint. Discussion started: 2 November 2026
© Author(s) 2026. CC BY 4.0 License.

uncertainty. Early satellite SWE retrieval algorithms relied primarily on passive microwave (PM) observations (Kelly et al., 2003; Durand et al., 2008). While PM sensors provide frequent, large-scale observations, their coarse spatial resolution results in mixed land-water pixels and large uncertainties over lakes. For example, current operational SWE products therefore simplify lake conditions by assuming fixed lake ice properties within Helsinki University of Technology (HUT) microwave emission models (Luojus et al., 2021), despite previous studies demonstrating that lake ice thickness substantially influences brightness temperature (Lemmetyinen et al., 2009; Gunn et al., 2011). Active microwave observations have also been explored, including C-band Sentinel-1 for snow retrieval under relatively deep snow conditions (Lievens et al., 2019). Nevertheless, both passive microwave and lower-frequency radar observations exhibit limited applicability to the shallow snowpacks commonly found on lake ice and provide only limited information on snow microstructure (Foster et al., 2005; Clifford, 2010).

Recent developments in snow remote sensing have increasingly focused on high-frequency radar, as it is more sensitive to both snow mass and microstructure (Tsang et al., 2021; King et al., 2015, 2018; Thompson et al., 2019). These advances were largely motivated by the proposed CoReH2O mission (Rott et al., 2010; Lemmetyinen et al., 2018) and the subsequent development of physically based SWE retrieval algorithms (Zhu et al., 2018; King et al., 2018; Thompson and Kelly, 2021a). At these radar frequencies, interpreting radar observations requires physically based electromagnetic (EM) models that describe volume scattering in complex snowpacks. Considerable progress has therefore been made in radiative transfer modelling to better represent snow microstructure and substrate effects (Colbeck, 1982; Meloche et al., 2021; Picard et al., 2022). Several microwave emission and scattering models, including Dense Medium Radiative Transfer (DMRT), Microwave Emission Model of Layered Snowpacks (MEMLS), and HUT, have been developed with varying levels of success (Lemmetyinen et al., 2010; Royer et al., 2017). Subsequent studies demonstrated that realistic representation of snow microstructure is the dominant factor controlling model performance (Löwe and Picard, 2015; Sandells et al., 2017; Vargel et al., 2020), leading to the development of the Snow Microwave Radiative Transfer (SMRT) model (Picard et al., 2018), a flexible and modular framework that has since been successfully applied across numerous terrestrial snow studies (Montpetit et al., 2024; Carletti et al., 2025; Gélinas et al., 2026), and has also shown success in modelling radar response from rough surfaces at high frequencies (Larue et al., 2021).

Despite these advances, radiative transfer modelling at high microwave frequencies has almost exclusively focused on terrestrial snow environments. Applications have primarily been conducted over tundra (Montomoli et al., 2015; Montpetit et al., 2024), vegetated landscapes (Woolley et al., 2026), and mid-latitude seasonal snowpacks (Thompson et al., 2019; Gélinas et al., 2026). In contrast, snow-covered lakes have received little attention due to their substantially different snow properties and underlying ice substrate. Existing radar forward modelling studies over ice have predominantly focused on lower-frequency satellite sensors operating from X to L-band (Murfitt et al., 2022, 2023, 2024; Fan et al., 2023; Wang et al., 2025). These studies showed that freshwater lake ice backscatter at lower-frequency radar is primarily controlled by ice-water interface roughness, whereas sea ice backscatter is dominated by ice surface roughness, with snow contributing only weakly at lower frequencies. Physical modelling of lake ice using high-frequency radar investigations remains limited, with

https://doi.org/10.5194/egusphere-2026-5457
Preprint. Discussion started: 2 November 2026
© Author(s) 2026. CC BY 4.0 License.

only a few studies examining Ku-band interactions over lake ice (Gunn et al., 2015), leaving the mechanism of high-frequency radar interactions on snow-covered lake ice largely unresolved.

The recent launch of the Surface Water and Ocean Topography (SWOT) mission provides a unique opportunity to investigate microwave interactions over snow-covered lakes. SWOT's Ka-band Radar Interferometer (KaRIn) operates at near-nadir incidence angles and was designed primarily to measure water surface elevation, but recent advances in estimating sea ice freeboard have demonstrated its application in the cryosphere (Kacimi et al., 2025; Müller et al., 2026). Correct interpretation of SWOT backscatter, therefore, requires a detailed understanding of electromagnetic wave interactions under near-nadir geometry. Although several recent studies have examined SWOT backscatter over snow-covered environments (Trudel et al., 2024; Veijola et al., 2024; Yoon et al., 2026; Mugunthan et al., 2026), a physical understanding of the interaction between the SWOT KaRIn sensor and snow/ice remains largely lacking. Furthermore, the bistatic interferometric capability of the KaRIn sensor presents additional opportunities for snow depth retrieval, as earlier interferometric approaches were limited by weak interaction at the snow-air interface from lower-frequency sensors (Rott et al., 2010) or by phase-wrap problems in monostatic interferometry (Belinska et al., 2024). Possibilities for retrieving ice/snow parameters using KaRIn remain largely unexplored because fundamental aspects of Ka-band propagation through snow-covered lake ice, particularly penetration depth, response to surface roughness, and surface scattering, are still poorly understood (Landy et al., 2026; Luo et al., 2026; Meloche et al., 2026; Mullet et al., 2026; Stroeve et al., 2026).

To address these knowledge gaps, this study applies the Snow Microwave Radiative Transfer (SMRT) model to investigate Ka-band backscatter over snow-covered lake ice observed by SWOT. Specifically, the objectives are to: (1) develop a physically based SMRT representation of snow-covered lake ice suitable for SWOT Ka-band observations; (2) evaluate simulated backscatter driven using in-situ measurements compared to SWOT KaRIn acquisitions; and (3) investigate the relative influence of snow, ice, and surface properties on Ka-band scattering using sensitivity analyses based on SMRT's simulation.

2 Data & Methods

2.1 Study Site: Kluane Lake and in-situ measurements

The study is centred on Lhù'ààn Mân (Kluane Lake), the largest lake in Yukon, located in the southwestern portion of Yukon Territory, shown in Figure 1 (61.283°N, 138.75°W). Situated at an elevation of 781 m above sea level, the lake covers a surface area of approximately 408 km with a mean depth of 31 m and a maximum depth of 91 m in the glacially influenced southern basin (Brahney et al., 2008; McKnight et al., 2021). The region has a continental subarctic climate, situated in the rain shadow of the St. Elias Mountains, resulting in semi-arid conditions with a mean annual temperature of -3.8 °C and low annual precipitation of around 300 mm (ECCC, 2021).

https://doi.org/10.5194/egusphere-2026-5457
Preprint. Discussion started: 2 November 2026
© Author(s) 2026. CC BY 4.0 License.

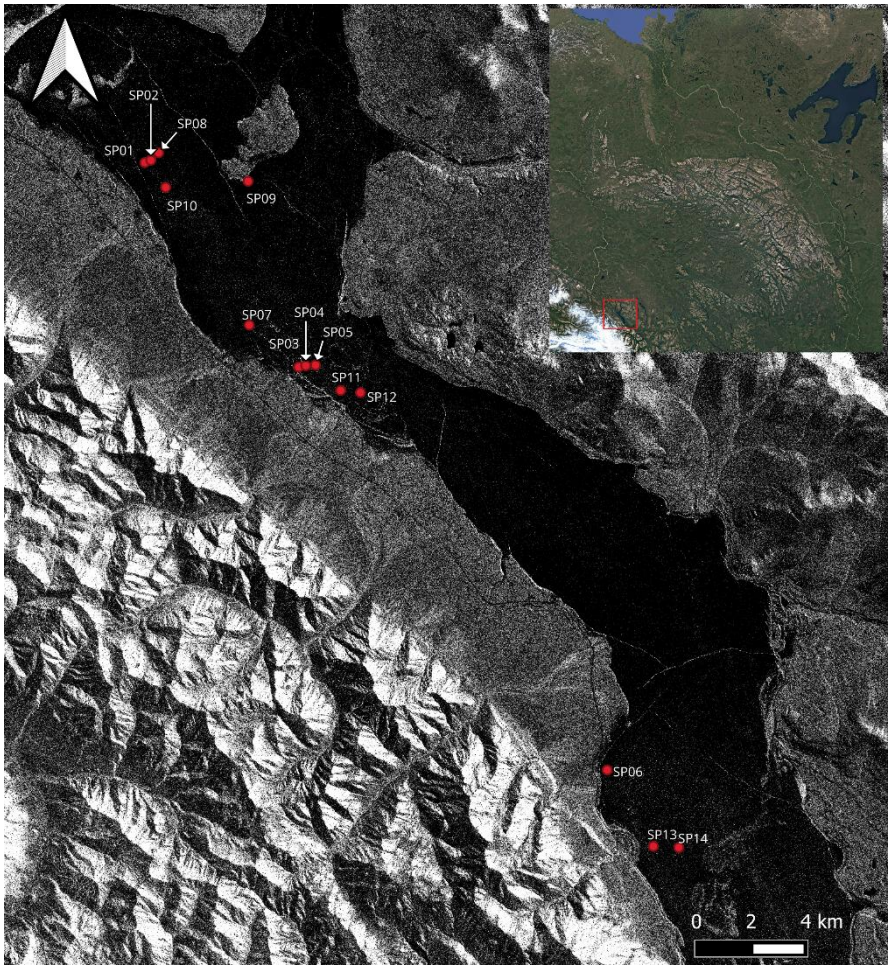


Figure 1: Location of Kluane Lake (61.283°N, 138.75°W), with an inset map of the Yukon Territory shown at the upper right. The location of snow pit measurements is shown as a red circle and labelled on the map using NISAR HH-polarization data (2026-01-01) as background, showing the lake ice conditions at the study site. The base map was designed and developed by Google.

To characterize the physical conditions governing microwave scattering, ice/snow measurements were collected over representative lake-ice surfaces during a field campaign in the 2026 winter season. Snow depth was measured using the SnowHydro Magnaprobe - an automated probe that records depth and GPS coordinates - in a spiral sampling strategy from the center point to a 20-meter radius, with measurements spaced every 1–2 meters (Sturm and Holgrem, 2018). Approximately 300-800 snow-depth samples were acquired and averaged at each site to capture small-scale variability in snow accumulation, which strongly influences Ka-band scattering. Magnaprobe measurements less than 5 mm were considered to be bare ice through the bias correction factor from the Magnaprobe metadata. At the center, a snow pit was excavated to obtain vertical profiles of key snow properties, with measurements taken at 3-cm intervals. Snow density ρ_{snow}

https://doi.org/10.5194/egusphere-2026-5457
Preprint. Discussion started: 2 November 2026
© Author(s) 2026. CC BY 4.0 License.

was measured for each stratigraphic layer using standard 100 cc cutters, while a stem thermometer recorded temperatures at multiple depths to characterize thermal gradients. The maximum extent of prevailing grain (D_{max}) and grain type were documented following established snow-classification protocols, using a 1-millimetre comparison card and a field microscope, and visually identifying the particle types in snow samples according to Fierz et al. (2009). D_{max} measurements of wind slab, faceted slab and depth hoar are around 0.5 mm, 1 mm and 2 mm in Kluane Lake, respectively. Also, multiple ice thickness measurements were observed for each site at the central point and at 20-meter spacing in the direction of each cardinal coordinate (N, S, E, W) using a calibrated ruler inserted into an augured hole.

2.2 SWOT Data

The Surface Water and Ocean Topography (SWOT) mission was launched in December 2022, and its science orbit at a 21-day repeat pass starts in July 2023. SWOT carries the Ka-band (35.75 GHz) Radar Interferometer (KaRIn), the first spaceborne wide-swath radar interferometer designed to provide high-resolution measurements of global surface water elevation (Fu et al., 2024). KaRIn uses two antennas separated by a 10 m boom to form a single-pass interferometer, enabling simultaneous retrieval of water surface elevation and radar backscatter over a swath extending approximately 50 km on either side of the satellite ground track, with a 20 km nadir gap. Unlike conventional side-looking synthetic aperture radar (SAR) systems, KaRIn observes the Earth's surface at near-nadir incidence angles with an across-swath viewing geometry of approximately 0.6° – 4.5° (Fjørtoft et al., 2014). The 100m Level-2 High Rate Raster Version D products were used to characterize the radar response over snow-covered freshwater lakes; the per-pixel incidence angle provided in the SWOT raster product was used to account for variations in KaRIn viewing geometry across the swath. Backscatter information in sigma naught (σ°) was extracted and converted to decibels in this study (SWOT, 2025).

Table 1. Different SWOT KaRIn raster products used in this study, with acquisition information.

Acquisition ID	Incidence Angle Range	Polarizations	Acquisition Date	Pass number
A01	3.45 – 3.87	HH	2026-02-25	330
A02			2026-03-18	
B01	3 – 4.38	VV	2026-02-25	319
B02			2026-03-18	
C01	3.73 – 4.38	HH	2026-02-26	347
C02			2026-03-19	
D01	0.43 – 0.7	VV	2026-03-08	052
E01	1.17 – 1.42	HH	2026-03-08	041

https://doi.org/10.5194/egusphere-2026-5457
Preprint. Discussion started: 2 November 2026
© Author(s) 2026. CC BY 4.0 License.

Table 2. Snow pit properties used in this study, with in-situ measurements summarized.

Snow Pit ID	Snow Depth (m)	Bare Ice %	Average Ice Thickness (m)	Date	Bulk Density (kgm^{-3})	Ice Lens?
SP01	0.17	0	1.09	3/5/2026	346	
SP02	0.175	0	1.14	3/6/2026	273	
SP03	0.112	6	1.1	3/9/2026	349	Yes
SP04	0.089	0	1.1	3/9/2026	352	Yes
SP05	0.072	0	1.1	3/9/2026	222	
SP06	0.025	32	1.26	3/10/2026	321	
SP07	0.091	0	1.03	3/11/2026	330	
SP08	0.17	0	1.14	3/12/2026	340	
SP09	0.216	0	0.83	3/13/2026	246	Yes
SP10	0.19	0	1.15	3/14/2025	334	
SP11	0.087	0	1.15	3/15/2026	318	
SP12	0.105	0	1.15	3/15/2026	322	
SP13	0.033	10	1.25	3/18/2026	366	
SP14	0.043	23	1.23	3/18/2026	280	

Table 3. Summary of snow pit sampling sites contained in each SWOT acquisition, with incidence angle recorded in degrees.

Snow Pit ID	A01	A02	B01	B02	C01	C02	D01	E01
SP01	3.87				3.73		0.43	
SP02	3.85				3.75		0.48	
SP03	3.75		4.4		4.32		0.65	
SP04	3.74		4.38		4.34		0.65	
SP05	3.72		4.36		4.38		0.66	
SP06	3.52		3.25					1.17
SP07	3.83		4.57		4.2			
SP08	3.83				3.76		0.6	
SP09	3.64				4		0.7	
SP10	3.84				3.82			
SP11	3.68		4.27				0.68	
SP12	3.64		4.22				0.69	
SP13	3.5		3.06					1.36
SP14	3.45		3					1.42

2.3 Forward Modelling

2.3.1 Snow Microwave Radiative Transfer Model

The Snow Microwave Radiative Transfer (SMRT) model is a modern, multilayer radiative-transfer framework designed to simulate brightness temperature and backscatter from snow, sea ice, and lake ice (Picard et al., 2018). The electromagnetic

https://doi.org/10.5194/egusphere-2026-5457
Preprint. Discussion started: 2 November 2026
© Author(s) 2026. CC BY 4.0 License.

and microstructure model determines the scattering and absorption properties of each snow/ice layer from its properties, while interface models calculate reflection and scattering at interfaces within the lake ice system based on their dielectric contrasts and surface-roughness characteristics. The radiative-transfer solver propagates the electromagnetic energy through the multilayer system and accounts for interactions between volume and interface scattering.

Different electromagnetic models can be used in SMRT for solving radiative transfer equations; the Dense Media Radiative Transfer Quasi-Crystalline Approximation (DMRT-QCA) has been used for lake ice studies in the past (Tsang et al., 1985; Gunn et al., 2015; Murfitt et al., 2023) for the purpose of representing bubbles in the ice column using the Sticky Hard Sphere (SHS) microstructure model. However, DMRT-QCA is only applicable when k_0a is under 0.6 (Picard et al., 2022b), where the wavenumber k_0 at the Ka-band is 0.75 $mm^{-1,}$ and a is the snow grain or bubble radius; this leads to any snow grain or bubble radius more than 0.8 mm violating the small-particle assumption underlying conventional DMRT-QCA formulations. The Improved Born approximation (IBA) has been demonstrated as a better electromagnetic model used in high-frequency microwave studies (Vargel et al., 2020), as it won't violate the small-particle assumption (Mätzler, 1998), and more snow microstructure models can be used in IBA, where correct snow microstructure representation has been a major consideration for snow forward modelling (Löwe and Picard, 2015). IBA treats snow as a heterogeneous ice–air medium and relates its scattering properties to the dielectric contrast and spatial correlation of the snow microstructure (Picard et al., 2018), where the microstructure is described using an autocorrelation function, with the corresponding power spectral density determining the characteristic spatial scales contributing to microwave scattering (Mätzler, 2002). The exponential autocorrelation has demonstrated its effectiveness with the IBA model for representing snow scattering (Vargel et al., 2020), where the exponential correlation length can be determined using specific surface area (SSA) or the maximum extent of prevailing grains:

$$l_{ex} = \kappa \frac{4(1 - \frac{\rho_{snow}}{\rho_{ice}})}{SSA\ \rho_{ice}} \quad (1)$$

$$l_{ex} = \begin{cases} 0.18 + 0.09 \ln(D_{max}), \frac{\rho_{snow}}{\rho_{ice}} > 0.2\ and\ D_{max} > 0.125\ mm \\ 0.05 \pm 0.017\ mm, otherwise \end{cases} \quad (2)$$

where l_{ex} is the exponential correlation length, D_{max} is the maximum extent of prevailing grains, ρ_{snow} and ρ_{ice} is the snow and ice density, respectively, and SSA is the specific surface area (m^2kg^{-1}), and κ is the polydispersity used as an empirical scaling factor. These relationships are based on empirical parameterization of Durand et al. (2008) and measurements reported by Mätzler (2002), such empirical conversions have also been applied in previous MEMLS-based snow studies (Li et al., 2025).

In addition to scattering within snow layers, microwave energy interacts with various interfaces or surfaces in the lake ice system: the snow surface, the ice surface, and the ice-water interface. Previous studies have concluded that Ku-band

https://doi.org/10.5194/egusphere-2026-5457
Preprint. Discussion started: 2 November 2026
© Author(s) 2026. CC BY 4.0 License.

radar altimetry will show quasi-specular scattering at the ice surface (or snow-ice interface) on sea ice (De Rijke-Thomas et al., 2023), indicating that interface roughness and incidence angle can strongly influence the observed radar response. Therefore, an appropriate representation of interface roughness is necessary to characterize the Ka-band backscatter from snow-covered lake ice. Current interface roughness models in SMRT can be categorized into two types: the Integration Equation Model (IEM) and the Geometrical Optics (GO) model (Fung and Chen, 1992; Tsang and Kong, 2001; Fung et al., 2002; Brogioni et al., 2010). The IEM-based formulation describes scattering from rough surfaces using Root-Mean-Square Height (RMS) deviations and the spatial correlation length (l_c), with the autocorrelation function determining the roughness spectrum. The Improved Integration Equation Model (IIEM) used in SMRT follows the formulation of Fung et al. (2002) and extends the applicable roughness regime of IEM by using transition Fresnel coefficients (Fung and Chen, 2004). The formulation calculates diffuse reflection and specular reflection, coherent transmission, and additional multiple-scattering terms (for cross-polarized returns). This extended treatment allows IIEM to be applied to surfaces with relatively large roughness or correlation lengths while retaining the integral-equation description of surface scattering. In contrast, the GO formulation applies to sufficiently rough surfaces where scattering is primarily governed by the distribution of local surface slopes, and the surface can be approximated as a collection of locally planar facets (Tsang and Kong, 2001).

After the scattering and absorption properties are calculated for each snow layer, along with the reflection and scattering properties of the surface interfaces, the results are combined using the radiative transfer equation (RTE) to simulate the propagation of microwave energy through the multilayer snow–ice system. In SMRT, the RTE is solved using the Discrete Ordinate and Eigenvalue Method (DORT), which discretizes the angular domain into a finite set of propagation streams and solves the coupled radiative-transfer equations for the multilayer medium (Picard et al., 2004). For active backscatter calculations, SMRT also provides an iterative second-order solver that separates the returned signal into contributions from different scattering mechanisms. The zeroth-order contribution represents reflection from the surface, interfaces, and substrate after attenuation through the snowpack, while the first-order terms include direct single-volume backscatter and interactions involving single-volume scattering events with interface or substrate reflections (Ulaby and Long, 2014). However, the first-order approximation might underestimate backscatter by neglecting multiple volume-scattering events, especially when the scattering albedo is high using a high-frequency radar sensor (Larue et al., 2021). To account for additional scattering interactions, the second-order solver extends the first-order formulation by explicitly calculating second-order scattering contributions following the successive-scattering framework of Karam et al. (1995). Also, the second-order solver implemented diagnostic backscatter contributions from individual layers, offering an advantage for physically interpreting the relative roles of the snow surface and layers, ice surface, and ice–water interface. This layer-resolved capability is particularly valuable in this study for identifying the dominant scattering pathways responsible for the observed Ka-band backscatter from lake ice.

https://doi.org/10.5194/egusphere-2026-5457
Preprint. Discussion started: 2 November 2026
© Author(s) 2026. CC BY 4.0 License.

2.3.2 Simulation Framework

Snow density, thickness, temperature, and stratigraphy data from the snow pit survey observed on Kluane Lake in March 2026 were used to construct snowpacks with the SMRT (Picard et al., 2018) model to validate our model configuration. Although several studies have indicated two-layered snowpack (Wind Slab and Depth Hoar) is sufficient in tundra environments (King et al., 2018; Montpetit et al., 2024), we configured a three-layered snowpack (Wind Slab, Faceted, and Depth Hoar) to represent snow microstructure because a considerable portion of faceted snow was observed during field sampling. The IBA EM model with exponential autocorrelation is used in this study based on its effectiveness in former snow studies (Mätzler 1998; King et al., 2018; Vargel et al., 2020; Montepetit et al., 2024; Welch and Kelly, 2025), where snow grain sizes were converted from D_{max} to exponential correlation length l_{ex} based on an empirical relationship (Mätzler 2002; Durand et al., 2008). Ice lenses were found in several snow pit sites and are modelled by inserting an extra snow layer between snowpacks, with a thickness of 2 mm, ρ_{snow} = 909 kg m^{-3}, and $l_{ex} = 3 \times 10^{-4}$ mm, which is converted from SSA = 100 m^{2}kg^{-1} (Sandells et al., 2024). Since snow depth can vary substantially within the SWOT radar footprint, individual observations may contain contributions from both snow-covered and snow-free portions of the lake ice. To account for this sub-footprint heterogeneity, backscatter is also simulated separately for snow-covered and bare-ice conditions, representing the two surface states. The simulated backscatter values were then weighted by the proportion of bare ice in each radar footprint, as derived from Table 2, to obtain a footprint-averaged backscatter representative of the observed SWOT measurement.

Interface roughness settings of Root Mean Square Height (RMS) deviations and Correlation length (l_c) at the ice-water Interface, the ice surface (or the ice-snow Interface), and the snow-air Interface between different sampling sites were assumed to be identical, based on interpretation during the field campaign that roughness characteristics at different snow pits do not exhibit large deviations. The IIEM was applied to the ice-water interface, the ice surface, and the snow surface under a smooth snow scenario (Fung et al., 2002). IIEM is valid when k × RMS < 3, where k is the wavenumber (~0.75 mm^{-1}) at Ka-band (Fung and Chen, 1992; Brogioni et al., 2010). Therefore, IIEM can be applied to the roughness interface when RMS is under 4 mm, which is reasonable for ice-water interface roughness levels in deep lakes (Murfitt et al., 2022). This study used several optimized roughness parameter settings of the ice -water interface based on previous modelled results (Gunn et al., 2011; Murfitt et al., 2023) and in situ-based studies (Bacal and Brown, 2026).

The ice-surface roughness is therefore optimized in this study because previous lake-ice modelling studies have demonstrated the importance of roughness but have not established a universal roughness parameter representative of freshwater ice across radar frequencies. Previous SMRT modelling on lake ice from Murfitt et al. (2022, 2023, 2024) investigated the influence of ice-interface roughness using multifrequency SAR observations and SMRT simulations, primarily at L-, C-, and X-band, with primary focus on roughness at the ice-water interface. Wakabayashi et al. (1999) derived ice-surface roughness using an in-situ roughness comb, but the snow removal process might introduce uncertainties in these measurements. In addition, roughness characteristics derived from sea ice cannot necessarily be directly transferred

https://doi.org/10.5194/egusphere-2026-5457
Preprint. Discussion started: 2 November 2026
© Author(s) 2026. CC BY 4.0 License.

to freshwater ice because sea-ice surfaces develop under different physical and structural conditions (Landy et al., 2019; Meloche et al., 2026). Therefore, we evaluated a range of RMS roughness and correlation-length configurations and compared their simulated backscatter with SWOT observations. Parameter configurations reported in previous in-situ based studies (Wakabayashi et al., 1999; Meloche et al., 2026) were also explicitly tested to determine whether they provide an acceptable representation of the observed Ka-band backscatter, rather than assuming that a new roughness configuration is required for freshwater ice.

GO were also used to represent the snow–air interface when snow is considered rough. The majority of snow surfaces observed during the field campaign were relatively smooth and were therefore represented using the smooth-snow configuration (Carletti et al., 2025). However, wind-driven redistribution also produced rougher snow surfaces such as sastrugi (Figure 2). To account for this variability, a rough-snow configuration was additionally simulated using the Geometrical Optics Backscatter (GO_B) model. Based on visual interpretation during the field campaign, the RMS of the rough snow surface is approximately 0.5–1 cm, which exceeds the valid range for IEM-based models. Hence, both smooth and rough snow scenarios were simulated in this study, with IIEM representing smooth snow and GO_B representing rough snow. The purpose of using GO_B instead of the original Geometrical Optics (GO) is that GO underestimates signal transmission into the snow layer, whereas GO_B is unaffected by this assumption because the microwave signal is assumed to be transmitted along the path of refraction, which has been used to characterize rough snow observed by low-resolution mode radar altimetry (Larue et al., 2021).



Figure 2. Ice and snow conditions at Kluane Lake, taken at SP01-central basin with 0.17m snow depth (Left) and SP06-south basin with 0.025m snow depth (Right). Small-scale wind-driven sastrugi were found to increase snow surface roughness; the ice surface is relatively smooth and composed of congelation ice, with roughness caused by a small amount of moisture that adheres to it and then freezes (Right).

https://doi.org/10.5194/egusphere-2026-5457
Preprint. Discussion started: 2 November 2026
© Author(s) 2026. CC BY 4.0 License.

Different IIEM autocorrelation functions were assigned to the three interfaces to reflect their distinct physical formation processes and expected spatial roughness characteristics (Fung and Chen, 1992). The ice–water interfaces are represented using an exponential autocorrelation function, based on protruding bubbles at the ice-water interface caused by tubular bubbles observed in previous studies (Gunn et al., 2018). In contrast, the snow-air interface and snow–ice interface were represented using a Gaussian autocorrelation function because smooth transitional roughness characteristics were found during the field campaign instead of occasional roughness, where these smooth characteristics at snow and ice surfaces can be observed in Wakabayashi et al. (1999) and Barella et al. (2026). The Gaussian autocorrelation function is also more efficient for radar-scale roughness at higher-frequency sensors where roughness scale is potentially larger than wavelength-dependent roughness parameters (Barella et al., 2026).

Ice columns were split into three layers of equivalent thickness, where the temperature of the top ice layer was estimated by field measurements (basal snow temperature), the bottom ice layer was assumed to be -2 °C, and the middle layer was estimated by averaging the top and bottom ice layers. Since no bubbled ice was observed in the Kluane Lake ice column (Figure 2), and the double-bounce effect from snow and tubular bubbles will be less effective at near-nadir incidence angle (Thompson and Kelly, 2021b), all ice layers were set to clear ice with the same parameters from Murfitt et al. (2023) using the SHS microstructure model. Table 4 summarizes all parameterizations defined in this section.

Table 4. Parameters of snow/ice properties used for SMRT simulation, obtained from in-situ measurements, optimization, and literature as described within brackets

Snow l_{ex} (Mätzler 2002; Durand et al., 2008; Montpetit et al., 2024)	
Wind Slab	0.06 mm
Faceted Slab	0.15 mm
Depth Hoar	0.23 mm
Ice-Water Interface Roughness (Gunn et al., 2011; Murfitt et al., 2023; Bacal and Brown, 2026)	
RMS	1 mm
l_c	5 cm
Ice Surface Roughness (Wakabayashi et al., 1999; Meloche et al., 2026)	
RMS	To be optimized
l_c	
Snow Surface Roughness: Smooth (Carletti et al., 2025)	
RMS	1 mm
l_c	5 cm
Snow Surface Roughness: Rough (Meloche et al., 2026)	
RMS	5 mm
l_c	25 cm
Ice Column (Murfitt et al., 2023)	
Porosity	1%
Stickiness	1

https://doi.org/10.5194/egusphere-2026-5457
Preprint. Discussion started: 2 November 2026
© Author(s) 2026. CC BY 4.0 License.

2.4 Normalized Percentage Change – Influence of Snow and Ice Parameters

A one-at-a-time Normalized Percentage Change (NPC) analysis similar to Murfitt et al. (2022) was conducted to quantify the relative influence of key snow and ice physical parameters on the simulated microwave backscatter, with the baseline configuration set by in-situ measurements and test ranges of parameters presented in Tables 4, 6, and 7. The ice surface roughness optimized in section 3.1 is used as the baseline parameter for the rest of the section. For each perturbation, the model was run to compute the corresponding change in the backscatter coefficient, and sensitivity was evaluated by the magnitude of the backscatter variation relative to the parameter change. Snow roughness characteristics in the rough snow scenario (GO_B) were converted to Mean Square Slope (MSS). To simplify the process, snow density were iterated with entire snowpack instead of each layer separately; For snow grain size, ϕ denotes a scaling factor applied to the baseline l_{ex}, with ϕ =1.5 corresponding to a 50% l_{ex} increase and ϕ =2 corresponding to a 100% l_{ex} increase, where ϕ ranges from 0.5 to 2 is usually considered minimum- maximum range of snow grain size polydispersity (King et al., 2018; Picard et al., 2022; Montpetit et al., 2024). The sensitivity was quantified using an NPC metric presented in Eq. 3, allowing comparison of the relative influence of different parameters on the simulated backscatter:

$$NPC = \frac{\frac{\sigma_i^\circ - \sigma_0^\circ}{\sigma_0^\circ}}{\frac{X_i - X_0}{X_0}} \quad (3)$$

where σ_i° is the linear backscatter iterated at a certain step (i), and σ_0° is the linear backscatter at the baseline configuration. X_i is the value of the parameter at the iterated step, and X_0 is the property value at the baseline configuration. If the NPC value is 0.5, this indicates that a 1% change in the corresponding snow/ice property will result in a 0.5% increase in backscatter (σ°). In addition, selected parameters were varied over a broader range to assess potential nonlinear responses and interactions. The results were then compared to identify which parameters exert the strongest control on backscatter magnitude as snow depth varies, thereby informing model calibration and prioritizing parameters that require accurate field characterization. Quartile thresholds calculated from all obtained absolute NPC values were used to classify the sensitivity of the different variables to backscatter.

3. Results

3.1 Ice surface roughness optimization & validation

The ice surface roughness was optimized by varying both the RMS height and correlation length of the snow–ice interface while keeping the remaining snowpack and ice properties fixed. As shown in Figures 3 and 4, the simulated backscatter exhibited a clear sensitivity to both roughness parameters. The lowest RMSE for the selected configuration was obtained with a roughness RMS of 1.25 mm and a l_c of 5 cm, yielding RMSE values of around 1.14 and 1.08 dB in smooth and rough snow scenarios, respectively. This parameter setting will be applied to the following sensitivity analysis in Sections 3.2 and 3.3. Also, roughness parameters used in former studies, such as structure-from-motion measurements by Meloche et al.

https://doi.org/10.5194/egusphere-2026-5457
Preprint. Discussion started: 2 November 2026
© Author(s) 2026. CC BY 4.0 License.

(2026) on flat first-year sea ice with RMS = 1.5 mm, l_c = 5 cm and Wakabayashi et al. (1999) roughness comb measurements on freshwater ice with RMS = 1 mm, l_c = 5 cm, also demonstrated satisfactory agreement when compared to SWOT backscatter. Using ice surface roughness parameters from Meloche et al. (2026) led to an RMSE of 1.23 in both smooth and 1.21 in rough snow scenarios, whereas the Wakabayashi et al. (1999) parameters led to an RMSE of 1.56 dB in smooth snow and 1.42 dB in rough snow. Two scatterplot matrices also indicate a clear dependence of the simulated backscatter on incidence angle. Differences in the SWOT incidence angle contribute to variations in both observed and simulated backscatter across acquisitions. For example, acquisition D01, with a near-nadir incidence angle (0.43°–0.7°) at the study site, showed higher simulated and observed backscatter than acquisition C02, which had a far-nadir incidence angle (3.73°–4.38°).

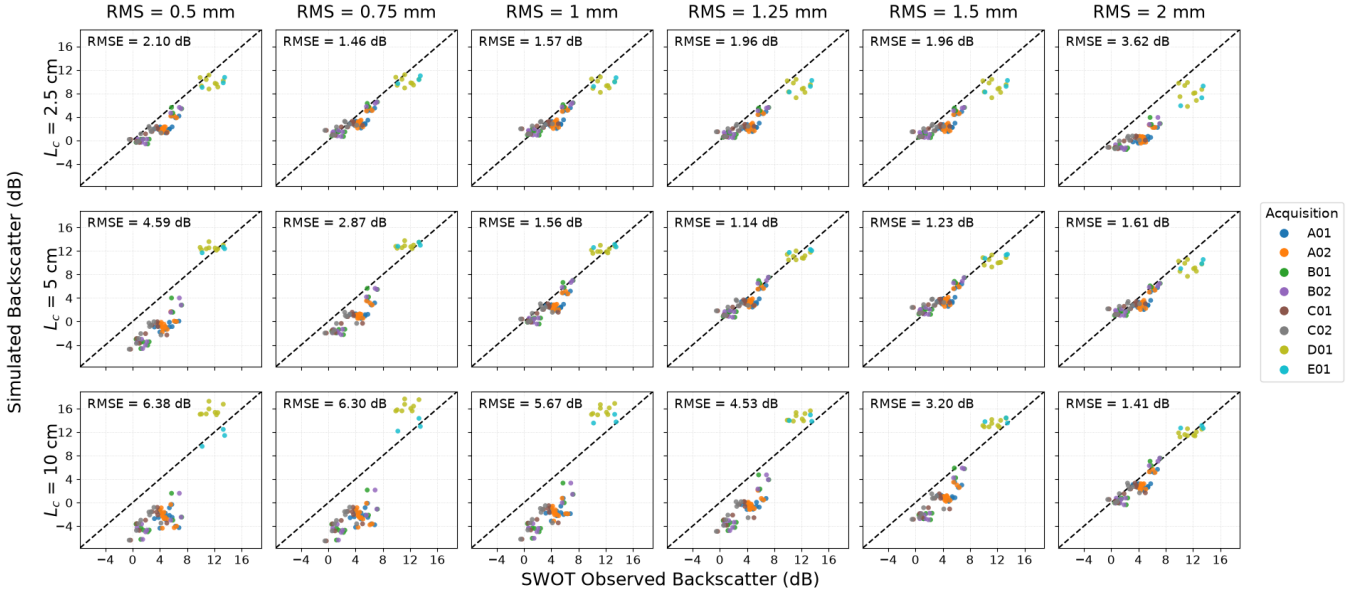


Figure 3. Optimization of ice surface roughness in smooth snow scenario (IIEM). Columns show RMS roughness (0.5 – 2.0 mm), and rows show correlation length l_c (2.5 – 10 cm). Colored points represent seven SWOT acquisitions.

The evaluation results using an ice surface RMS of 1.25 mm and l_c of 5 cm demonstrate the best overall agreement between the SMRT simulations and SWOT observations at both snow surface scenarios across the different acquisitions, shown in Table 5. The combined results show an overall RMSE of 1.14 and 1.08 for smooth and rough snow scenarios, respectively, with a high Pearson correlation coefficient of 0.95, indicating that the simulations capture the variability of the backscatter between different snow pits and SWOT acquisitions well. The acquisition-level results show some variation in model performance. The strongest agreement is observed for B01 and B02, which have RMSE values below 1 dB and correlation coefficients of approximately 0.97, where scatterplots in Figure 5 also demonstrate that acquisitions B01 and B02 have the best agreement. The D01 and E01 acquisitions, which were combined due to limited samples and their similar

https://doi.org/10.5194/egusphere-2026-5457
Preprint. Discussion started: 2 November 2026
© Author(s) 2026. CC BY 4.0 License.

incidence-angle ranges and acquisition dates, exhibit a lower correlation (approximately 0.45–0.48), although their RMSE remains close to 1.1 dB.

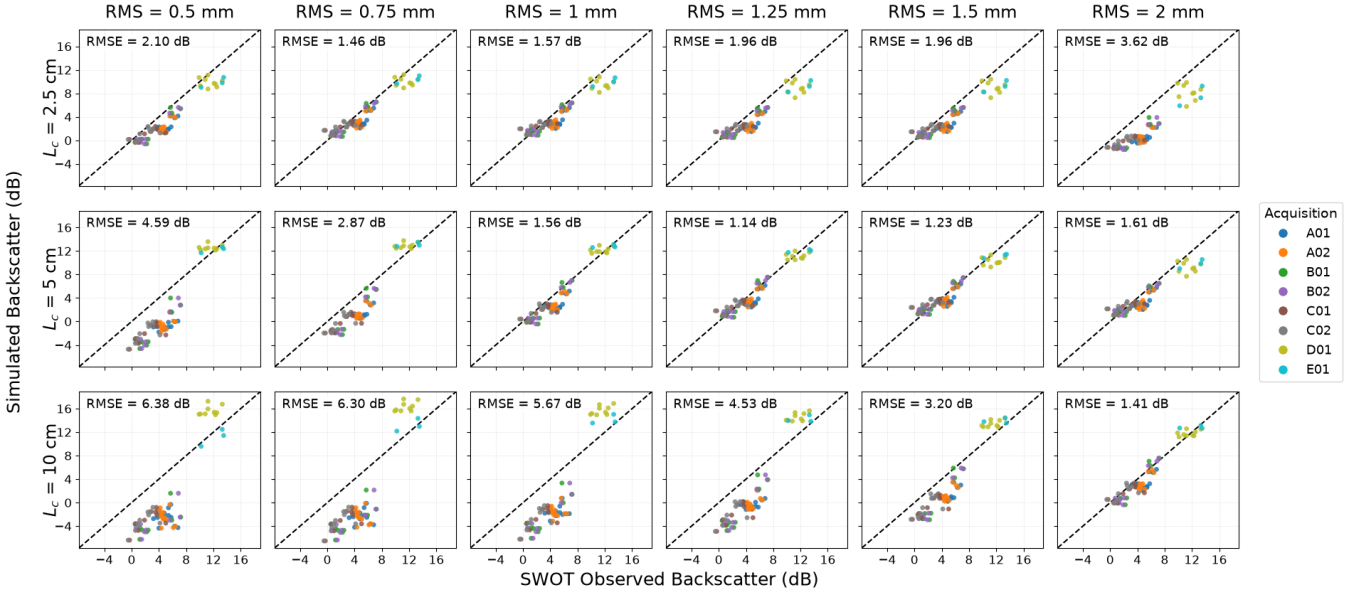


Figure 4. Optimization of ice surface roughness in rough snow scenario (GO_B). Columns show RMS roughness (0.5 – 2.0 mm), and rows show correlation length l_c (2.5 – 10 cm). Colored points represent seven SWOT acquisitions.

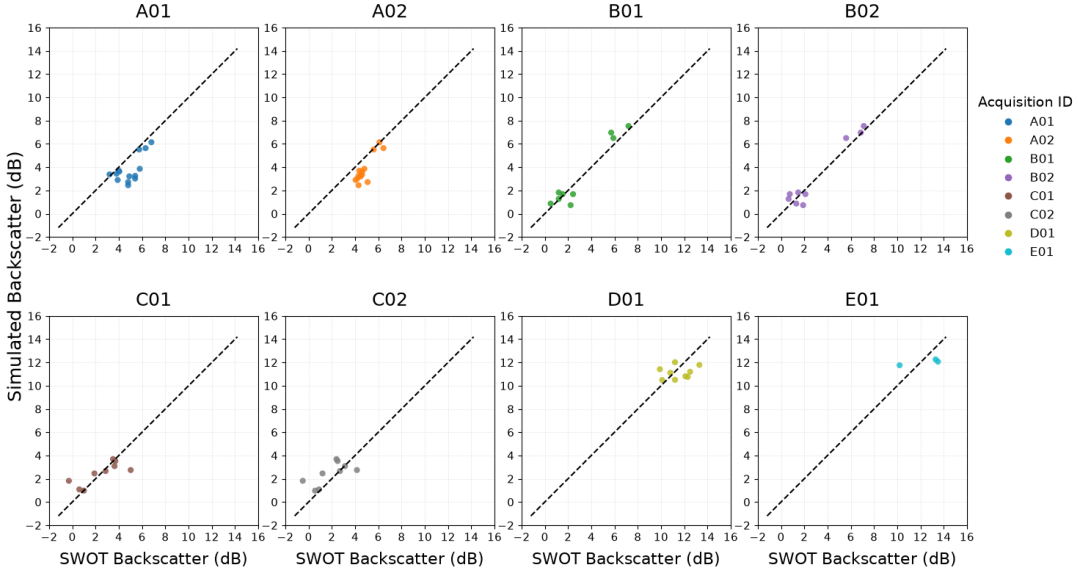


Figure 5. Scatterplots of SWOT-observed and SMRT-simulated backscatter using optimized ice roughness parameters (RMS = 1.25mm, l_c = 5cm) for individual acquisitions in the smooth snow scenarios (IIEM), rough snow scenario (GO_B) can be found in Appendix Figure A1

https://doi.org/10.5194/egusphere-2026-5457
Preprint. Discussion started: 2 November 2026
© Author(s) 2026. CC BY 4.0 License.

Table 5. Evaluation of SMRT simulation in both smooth (IIEM) and rough (GO_B) snow scenarios based on scatterplots in Figure 5, with RMSE, Pearson correlation, and MBE values between image acquisitions. D01 and E01 were combined due to limited samples; they are in a similar incidence-angle range and were acquired on the same date.

Acquisition ID	RMSE (dB)		Correlation		MBE (dB)	
	IIEM	GO_B	IIEM	GO_B	IIEM	GO_B
A01	1.44	1.2	0.66	0.67	-1.15	-0.83
A02	1.21	0.96	0.88	0.87	-1.04	-0.72
B01	0.78	0.97	0.96	0.96	0.13	0.35
B02	0.68	0.82	0.97	0.97	0.14	0.37
C01	1.09	1.08	0.78	0.78	0.02	0.25
C02	1.14	1.27	0.68	0.69	0.55	0.79
D01 & E01	1.2	1.16	0.41	0.45	-0.35	-0.24
Total	1.14	1.08	0.95	0.95	-0.35	-0.11

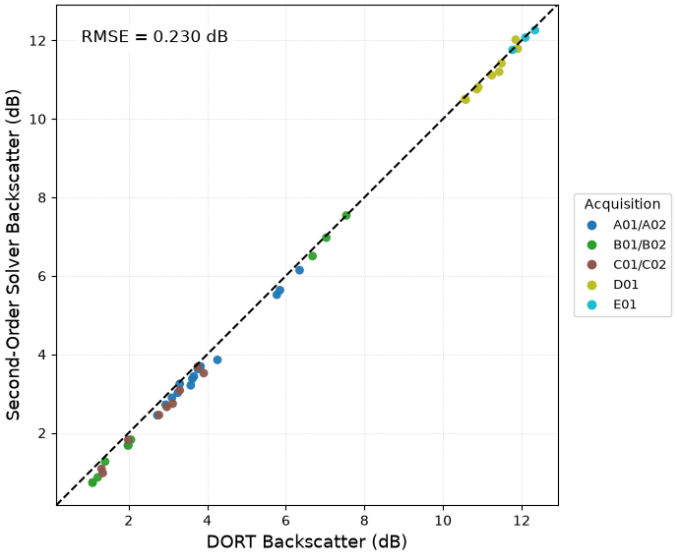


Figure 6. Comparison between DORT-simulated backscatter and Second-Order Solver-simulated backscatter for a smooth snow scenario .

The RTE was solved using two independent numerical approaches available in SMRT: DORT and the Second-Order Iterative Solver. DORT discretizes the angular domain into a finite number of propagation streams and solves the coupled radiative-transfer equations for the multilayer snow–ice system. The numerical convergence of the DORT solution depends on both the number of streams ($n_{streams}$) and the number of azimuth modes (m_{max}). Increasing $n_{streams}$ provides finer angular discretization and is particularly important for the near-nadir simulations because the returned energy can be concentrated within a relatively narrow angular range. In addition, a sufficiently large m_{max} is required for the IIEM-based interface scattering formulation due to IIEM's strong peakiness in the forward scattering direction, which represents the

https://doi.org/10.5194/egusphere-2026-5457
Preprint. Discussion started: 2 November 2026
© Author(s) 2026. CC BY 4.0 License.

rough-surface scattering field through an angular expansion and therefore requires sufficient expansion terms to accurately resolve the scattering contribution. Consequently, both $n_{streams}$ and m_{max} were progressively increased to accurately simulate Ka-band backscatter by DORT; increasing these parameters also increases computational demand cubically.

The comparison between the proposed second-order solver and the DORT solution demonstrates the precision of the second-order approximation across the tested acquisition conditions with DORT (Figure 6). Only the smooth snow scenario (IIEM) was compared here because DORT does not support the GO_B interface model for the rough snow scenario. For the DORT simulations, the numerical parameters were increased to $n_{streams} = 128$ and $m_{\max} = 50$ to achieve convergence under acceptable computational complexity. The simulated backscatter values show close correspondence to the DORT results, with an overall RMSE of 0.24 dB, driven by underestimation of the second-order solution by around 0–0.3 dB. This behaviour is physically plausible because the second-order solver accounts for scattering contributions only up to the second order (Karam et al., 1995). Also, DORT results showed a tendency to overestimate the simulated backscatter, where this overestimation could be reduced by further increasing $n_{streams}$. However, doing so would substantially increase computational demand and was considered impractical for the large number of simulations required in this study. Consequently, the small negative deviation from the 1:1 relationship is consistent with the expected contribution of higher-order scattering to the total backscatter, demonstrating that simulation results from the second-order solver can be used to characterize DORT results, derive more useful information, and improve computational efficiency.

3.2 Normalized Percentage Change

An NPC analysis is conducted to quantify the sensitivity of the simulated Ka-band backscatter to variations in snow and lake-ice properties under different observations and surface conditions (Table 8). The analysis considered three representative lake-ice scenarios: thick snow cover using a 3-layer snowpack (30 cm), thin snow cover using a 1-layer snowpack (5 cm), and snow-free lake ice, with incidence angles of 1°, 3°, and 5° selected to represent the near-nadir geometry of SWOT KaRIn. Based on snow stratigraphy we observed at the Kluane Lake field campaign, a 3-layer snowpack is constructed for a thick snow scenario, where the snowpack is separated into three equal-thickness layers to represent Wind Slab, Faceted, and Depth Hoar, and a 1-layer snowpack is constructed for a thin snow scenario, which only contains Wind Slab. For snow-covered conditions, both the smooth-snow configuration using IIEM and the rough-snow configuration using the GO_B formulation are evaluated. The resulting NPC values from the two snow-surface configurations are averaged across the thick- and thin-snow scenarios to provide a more concise representation of parameter sensitivity. The snow surface parameters, namely smooth-snow RMS height, smooth-snow l_c and rough-snow MSS, were excluded from this averaging because they are unique to their respective surface representations. Also, only the VV polarization is included in the analysis and the rest of the sections because SMRT-simulated backscatter differences between the two polarizations are less than 0.05 dB.

https://doi.org/10.5194/egusphere-2026-5457
Preprint. Discussion started: 2 November 2026
© Author(s) 2026. CC BY 4.0 License.

Table 6. Baseline configuration for SMRT sensitivity analysis; remaining parameters from other snow/ice properties will be identical to Table 4. WS = Wind Slab, FS = Faceted Slab, DH = Depth Hoar.

Parameter	Bare Ice	Thin Snow (1-layer snowpack)	Thick Snow (3-layer snowpack)
Ice Thickness	1.1 m		
Ice Surface Temperature	-15 °C		
Ice Surface RMS	1.25 mm		
Ice Surface l_c	5 cm		
Snow Depth		5 cm	30 cm
Snow Temperature		-15 °C	
Rough Snow MSS		0.8×10^{-3}	
Snow Density (WS/FS/DH)		300 kgm^{-3} (WS only)	300/250/250 kgm^{-3}
Snow l_{ex} (WS/FS/DH)		0.06 mm (WS only)	0.06/0.15/0.23 mm

Table 7. Ranges used for different snow/ice properties for NPC analysis; values given in brackets are interval values between each iteration. WS = Wind Slab, FS = Faceted Slab, DH = Depth Hoar.

Ice Thickness	0.1 – 1.5 (0.2) m
Ice Temperature (Top)	-25 - -5 (2) °C
Ice-Water Interface RMS	0.2 – 2 (0.2) mm
Ice-Water Interface l_c	1 – 10 (1) cm
Ice Surface RMS	0.25 – 2 (0.25) mm
Ice Surface l_c	2 – 14 (2) cm
Snow Depth (Thick)	5 – 50 (5) cm
Snow Depth (Thin)	1 – 10 (1) cm
Snow Temperature	-25 - -5 (2) °C
Smooth Snow Surface RMS	0.2 – 2 (0.2) mm
Smooth Snow Surface l_c	2 – 20 (2) cm
Rough Snow Surface MSS	0.5×10^{-3} – 5×10^{-3} (0.5×10^{-3})
Snow Density (WS) Snow Density (FS) Snow Density (DH)	250 – 350 (10) kgm^{-3} 200 – 300 (10) kgm^{-3} 200 – 300 (10) kgm^{-3}
Snow l_{ex} scaling factor ϕ	0.5 – 2 (0.1)

The results demonstrate that the sensitivity of Ka-band backscatter varies substantially among the investigated snow and ice properties. As shown in Table 8, ice surface RMS, l_c, and snow density resulted in the highest average NPC values of 0.88, 0.73, and 0.42. Snow depth (0.08), snow grain size (0.26), ice thickness (0.11), and snow surface roughness (0.12 – 0.21) exhibit moderate NPC values. In contrast, ice temperature (0.003). Snow temperature (0.02) and ice–water interface roughness (0.01–0.03) show relatively low sensitivity within the tested parameter ranges. The sensitivity also varies with snow conditions; it is less meaningful to interpret NPC values as indicating greater or lower sensitivity between different incidence angles or between snow-covered and snow-free scenarios, since NPC is normalized by the baseline linear backscatter, and differences in baseline backscatter magnitude among observation and surface conditions can substantially

https://doi.org/10.5194/egusphere-2026-5457
Preprint. Discussion started: 2 November 2026
© Author(s) 2026. CC BY 4.0 License.

affect the resulting relative change. However, it is evident that deep and shallow snow showed more pronounced differences in NPC values with respect to snow density, grain size, and depth, with the deep snow scenario exhibiting greater sensitivity. To avoid bias, the effects of incidence angle and snow-cover scenarios on the magnitude and response of Ka-band backscatter are examined separately; a more in-depth examination is presented in Section 3.3.

Table 8. Absolute Average NPC of simulated SWOT Ka-band backscatter in different snow/ice properties, where Ice RMS and Ice l_c represent roughness parameters at the ice surface

	Thick Snow			Thin Snow			Bare-Ice			
	1°	3°	5°	1°	3°	5°	1°	3°	5°	Average
Ice Thickness	0.053	0.081	0.184	0.085	0.125	0.282	0.022	0.039	0.116	0.110
Ice Temperature	0.001	0	0.007	0	0.001	0.01	0.005	0.003	0.002	0.003
Ice-Water Interface RMS	0.033	0.022	0.042	0.053	0.034	0.065	0.014	0.011	0.027	0.033
Ice-Water Interface l_c	0.017	0.009	0.008	0.027	0.013	0.012	0.007	0.004	0.005	0.011
Ice RMS	0.63	0.38	1.003	0.78	0.43	1.18	0.858	0.708	1.96	0.881
Ice l_c	0.705	0.3	0.64	0.85	0.33	0.75	1.121	0.52	1.336	0.728
Snow Temperature	0.02	0.027	0.033	0.005	0.007	0.008				0.017
Flat Snow RMS	0.31	0.167	0.196	0.28	0.14	0.14				0.206
Flat Snow l_c	0.293	0.156	0.187	0.26	0.13	0.16				0.198
Rough Snow MSS	0.16	0.06	0.18	0.14	0.05	0.14				0.122
Snow Density	0.2	0.505	0.65	0.2	0.45	0.51				0.419
Snow Grain size l_{ex}	0.51	0.61	0.43	0.008	0.01	0.007				0.263
Snow Depth	0.115	0.14	0.15	0.02	0.02	0.02				0.078

NPC Classification: No/Low (0 - 0.017) Medium (0.018 - 0.121) High (0.122 - 0.31) Very High (> 0.31)

3.3 Sensitivity analysis

Unlike the NPC analysis, which provides a normalized measure of relative parameter sensitivity, this section explicitly evaluates how changes in individual properties affect the magnitude and angular response of backscatter under contrasting snow and ice conditions. Simulations are first performed over the range of incidence angles considered in the SWOT observations and for representative thick-snow (30 cm with a 3-Layer snowpack), thin-snow (5 cm with a 1-Layer snowpack), and snow-free bare ice scenarios. Attention was given to properties identified as relatively influential in the NPC analysis, such as ice surface roughness, snow density, snow depth, and snow microstructural properties. The sensitivity analysis in this section also considers potential interactions among selected properties, allowing changes in backscatter to be evaluated within the coupled snow–ice system rather than as independent responses.

Beyond simulating total backscatter at varying incidence angles, the analysis is extended from total backscatter to the backscatter contribution from layer volume scattering and at interfaces, inspired by applications of second-order iterative solvers. Since the second-order solver in SMRT assigns backscatter from volume scattering plus the corresponding lower

https://doi.org/10.5194/egusphere-2026-5457
Preprint. Discussion started: 2 November 2026
© Author(s) 2026. CC BY 4.0 License.

boundary interface to each layer, layer configurations were reconstructed to isolate the contributions of the snow volume, snow surface and ice interfaces. The lowermost 0.5 cm of snow was extracted to represent the contribution from the snow–ice interface; for the 1-Layer snowpack representing the thin-snow scenario, the properties of this layer were set to those of the wind slab, whereas for the 3-Layer snowpack representing the thick-snow scenario, they were set to those of the depth-hoar layer. Then, the lowermost 0.5 cm of lake ice was extracted to isolate the contribution from the ice–water interface, with its ice properties assumed to be identical to those of the overlying ice column.

3.3.1 Incidence angle

The layer-resolved backscatter contributions demonstrate a clear dependence on incidence angle and snow cover condition in Figure 7. In the bare-ice configuration, the total backscatter is composed of the ice-surface and ice–water interface contributions, with the ice-surface contribution closely following the total backscatter across the incidence-angle range. For the snow-covered cases, the snow-surface contribution is comparable to the ice-surface contribution near nadir (0° - 2°). However, backscatter from the snow surface decreases more rapidly than ice-surface backscatter as the incidence angle increases, resulting in the ice-surface contribution becoming increasingly dominant between approximately 2° and 5 °. The ice–water interface contribution also decreases with increasing incidence angle but remains relatively lower than the snow-surface or ice-surface contributions throughout the tested range. Increasing snow depth from thin to thick snow produces a noticeable increase in snow-volume backscatter, while this contribution varies relatively little with changes in incidence angle. Interestingly, the ice–water interface contribution is greater for the thin-snow scenario than for the bare-ice scenario, and this backscatter contribution decreased when switching from the thin-snow to the thick-snow scenario.

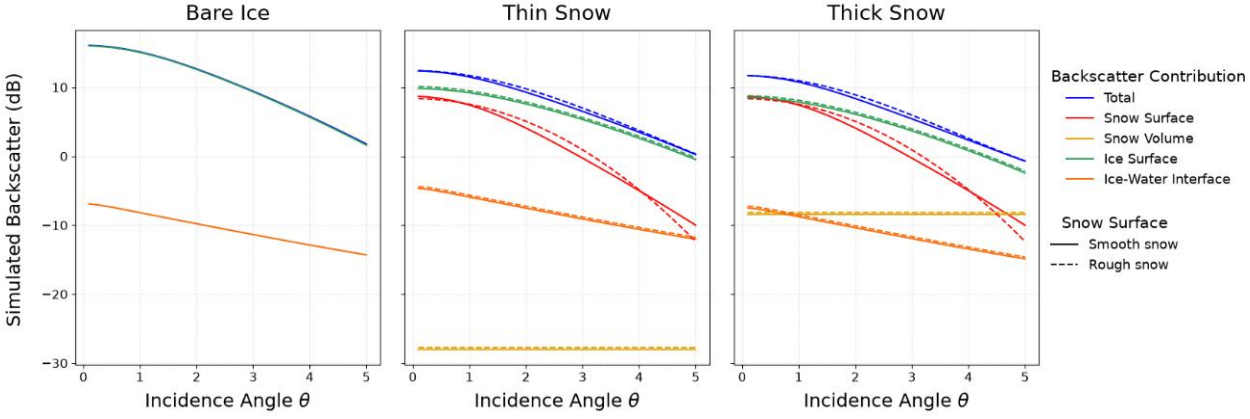


Figure 7. Backscatter contribution of each layer/interface of simulated Ka-band backscatter at varying SWOT incidence angle across different snow cover scenarios

https://doi.org/10.5194/egusphere-2026-5457
Preprint. Discussion started: 2 November 2026
© Author(s) 2026. CC BY 4.0 License.

3.3.2 Snow Depth

Based on Figure 8, Ka-band sensitivity to snow depth causes a consistent decrease in simulated backscatter coincident with snow thickening across all snowpack configurations and incidence angles, and a considerable decrease in backscatter from snow-off clear ice to snow-covered ice can be observed. The magnitude of this backscatter decrease in snow accumulation on snow-covered ice is strongly dependent on snow microstructure, particularly the characteristic of snow grain size represented by l_{ex}, where the scaling factor ϕ was used to configure the change of snow grain size in l_{ex}. As l_{ex} increases, the simulated backscatter declines more sharply with increasing snow depth. This effect is particularly evident in the three-layer snowpack configuration, which contains larger-grained snow layers at depth hoar compared to the single-layer configuration. The 3-layer snowpack under the thick-snow scenario, therefore, showed stronger depth-dependent attenuation of backscatter, especially for the larger l_{ex} scenarios. Notably, for the three-layer snowpack with ϕ = 1.5 and ϕ = 2, the decrease in backscatter begins to saturate at snow depths of approximately 30 cm, with the rate of attenuation progressively decreasing as snow depth increases. In contrast, the single-layer snowpack shows a more gradual decrease in backscatter as snow depth increases, with the effect of the grain-size scaling factor ϕ remaining comparatively limited. The results also demonstrate a clear incidence-angle dependence, with higher incidence angles generally producing lower backscatter and a more pronounced decrease with increasing snow depth at larger l_{ex}. The difference between the smooth (IIEM) and rough (GO_B) snow scenario is relatively small for most conditions.

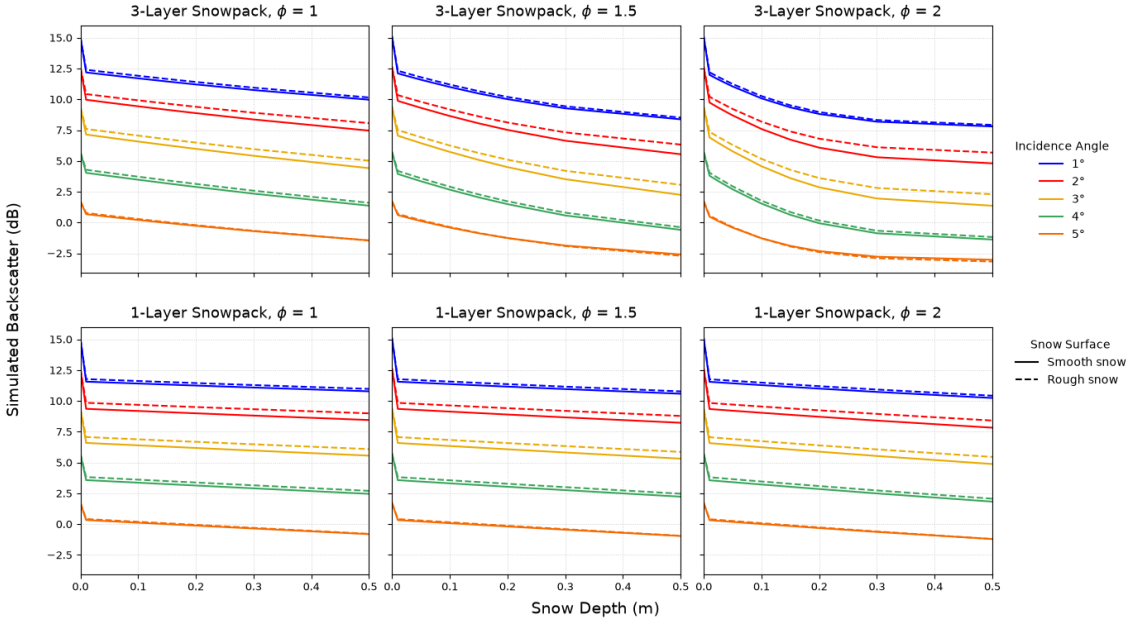


Figure 8. Sensitivity Analysis on Snow Depth at varying SWOT incidence angle, and its interaction with snow grain size variations characterized by a scaling factor ϕ.

https://doi.org/10.5194/egusphere-2026-5457
Preprint. Discussion started: 2 November 2026
© Author(s) 2026. CC BY 4.0 License.

The layer-resolved results at a fixed 3° incidence angle in Figure 9 provide further insight into the mechanisms underlying the snow-depth sensitivity shown above. As snow depth increases, the ice-surface and ice–water interface contributions both decrease linearly, with the reduction becoming more pronounced for larger snow grain sizes using a greater scaling factor ϕ. In contrast, the snow-volume contribution increases with increasing snow depth, reflecting the progressively greater contribution from volume scattering within the snowpack. This increase is strongest for larger l_{ex} and approaches a saturation level at approximately −5 dB. The corresponding decrease in the underlying ice-surface and ice–water interface contributions indicates increasing attenuation of radiation propagating through the snowpack, which is enhanced by larger snow grain sizes.

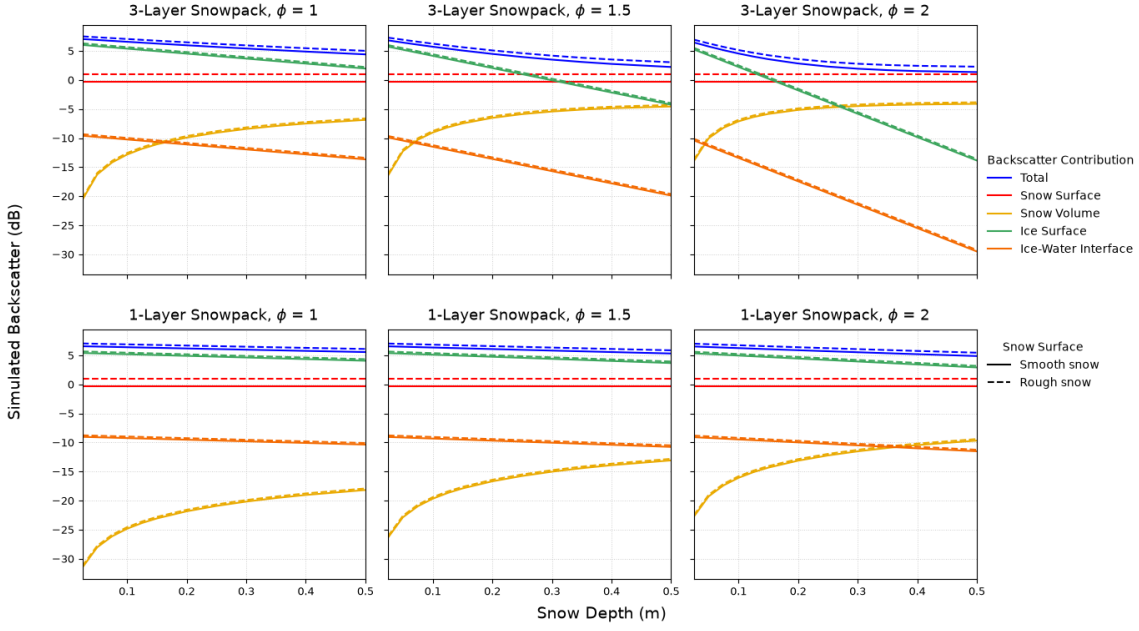


Figure 9. Backscatter contribution of simulated Ka-band backscatter at fixed 3° incidence angle, varying with snow depth and snow grain size, characterized by a scaling factor ϕ

3.3.3 Ice Thickness and Ice-Water Interface

The sensitivity analysis in Figure 10 indicates that simulated SWOT backscatter responds weakly to ice thickness once the ice layer becomes sufficiently thick (1 meter), with the strongest response occurring at relatively thin ice. Across all three snow-cover scenarios and incidence angles, backscatter decreases more rapidly at first as ice thickness increases, then gradually approaches a near-stable value. This behaviour is most pronounced at the 4 °- 5 ° incidence angle, where the decrease in backscatter is relatively large. Figure 11, which analyzes the backscatter contribution at different layers, also demonstrates that the decrease in backscatter is due to ice thickening at the ice-water interface.

https://doi.org/10.5194/egusphere-2026-5457
Preprint. Discussion started: 2 November 2026
© Author(s) 2026. CC BY 4.0 License.

The Ka-band simulations of roughness RMS at the ice-water interface are presented in Figure 12. At a thicker ice thickness of 1.1 m (baseline ice thickness), variations in both interface RMS roughness produce relatively small changes of less than 0.5 dB. In contrast, for thinner ice (0.1 m), the backscatter becomes substantially more sensitive to both RMS roughness, with changes in backscatter of at most 4 dB. The response to RMS roughness is particularly pronounced when snow is covered compared to the bare ice scenario, especially in the thin snow scenario. For the correlation length l_c the sensitivity to total backscatter is also stronger at thin ice compared to thick ice in all SWOT incidence angles, which can be found in Appendix Figure A2. Layered-resolve results in Figure 13 also illustrate an increase in backscatter contribution and stronger sensitivity from the ice-water interface at 0.1 m ice thickness during the thin snow scenario, leading to an increase in total backscatter (layer-resolve contributions at the ice-water interface in other snow cover scenarios can be found in Appendix Figure A3 and Figure A4 of this study).

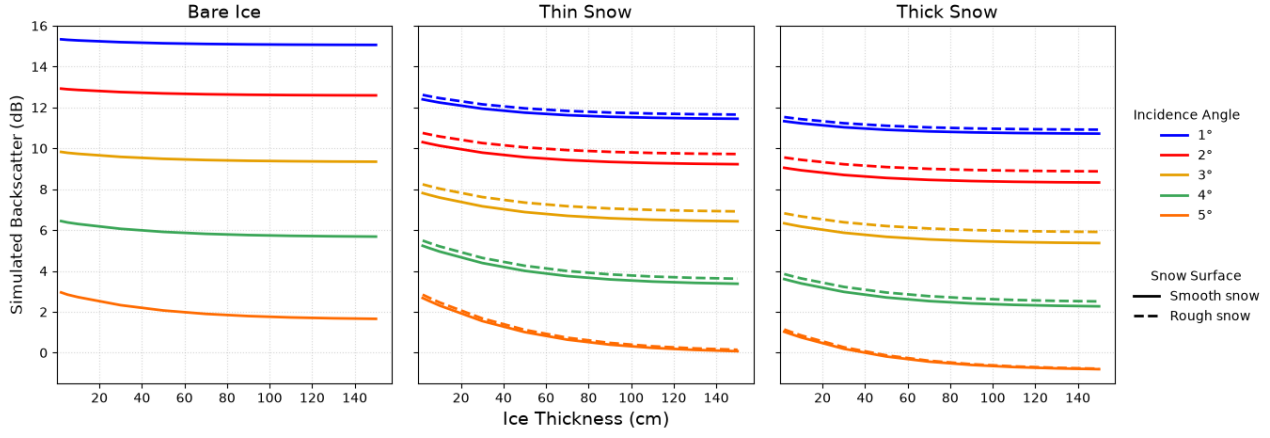


Figure 10. Sensitivity Analysis on Ice Thickness at varying SWOT incidence angle and snow cover scenarios

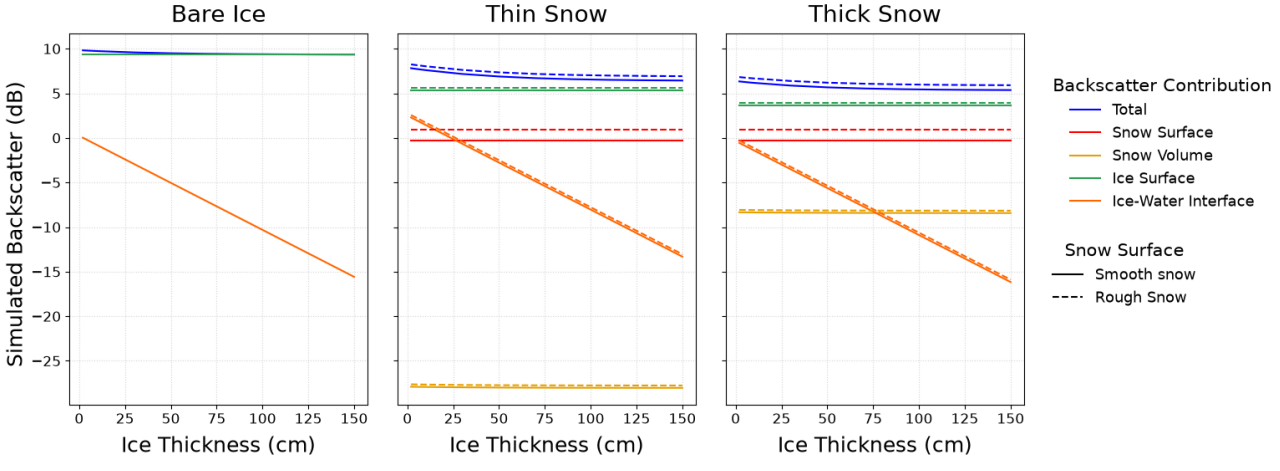


Figure 11. Backscatter contribution of simulated Ka-band backscatter at a fixed 3° incidence angle, varying with ice thickness and snow cover scenarios

https://doi.org/10.5194/egusphere-2026-5457
Preprint. Discussion started: 2 November 2026
© Author(s) 2026. CC BY 4.0 License.

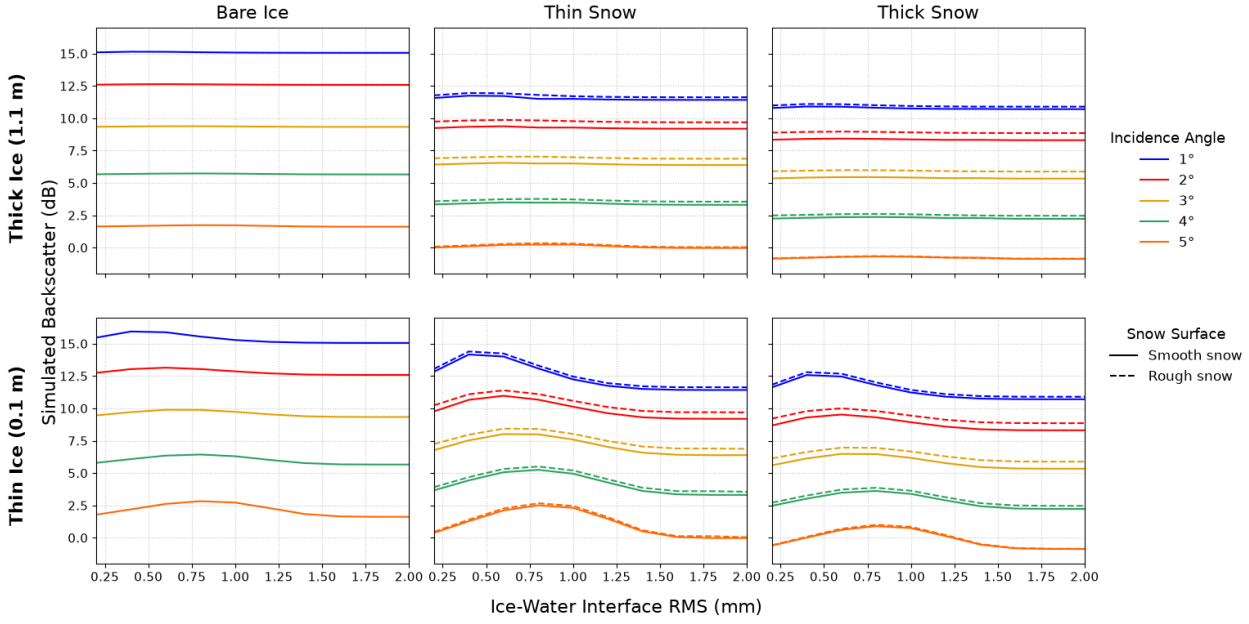


Figure 12. Sensitivity analysis of the ice-water interface RMS at different snow scenarios, with comparison between thick (1.1 m ice thickness) and thin ice (0.1 m ice thickness).

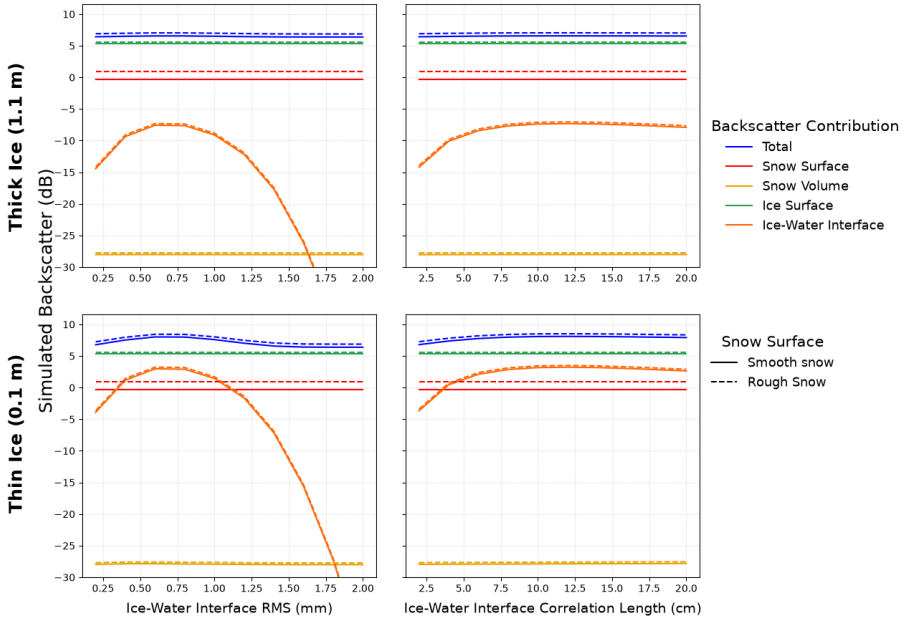


Figure 13. Backscatter contribution from Ice-Water interface roughness at a fixed 3° incidence angle and thin snow scenario, varied with thick (1.1 m ice thickness) and thin ice (0.1 m ice thickness).

https://doi.org/10.5194/egusphere-2026-5457
Preprint. Discussion started: 2 November 2026
© Author(s) 2026. CC BY 4.0 License.

3.3.4 Ice Surface Roughness

The ice-surface roughness properties illustrated in Figure 14 have demonstrated considerable influence on simulated Ka-band backscatter at the SWOT 3° incidence angle, with substantial changes in backscatter resulting from relatively small variations in both RMS roughness and correlation length. This considerable backscatter change is also shown in other SWOT angles illustrated in Appendix Figure A5. For RMS roughness, the response is generally nonlinear and strongly dependent on incidence angle. Under bare-ice conditions, increasing RMS roughness from 0.2 to approximately 0.8–1.2 mm produces a pronounced increase in backscatter, after which the response gradually levels off at larger RMS values. The backscatter sensitivity to the ice l_c is also considerable. Under snow-covered conditions, the response is generally less pronounced, but substantial variations remain, demonstrating that the horizontal spatial scale of the ice-surface roughness can strongly influence the Ka-band return. An interesting observation is that, based on backscatter contribution analysis at each layer, increasing the RMS of the ice surface leads to a monotonic decrease in backscatter from the ice-water interface, whereas the backscatter response from the ice surface is non-monotonic. Also, the increase in ice surface correlation length only modifies the ice surface contribution, while contributions from the ice-water interface stay constant. Overall, the results demonstrate that both the amplitude and spatial scale of ice-surface roughness can exert a stronger influence on Ka-band backscatter than several of the snow and ice properties examined previously.

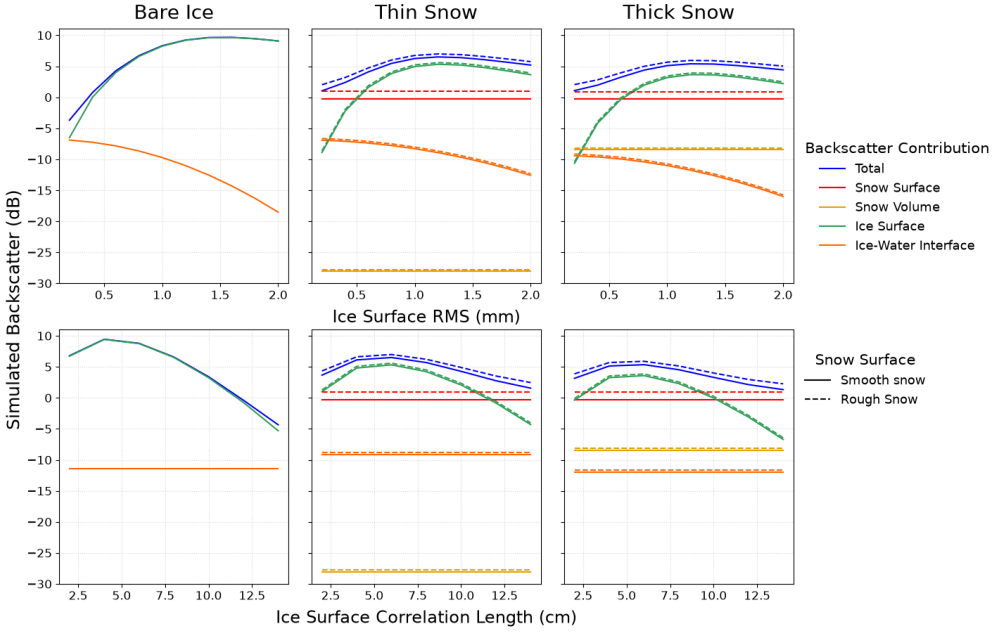


Figure 14. Ice Surface Backscatter contribution at fixed 3° incidence angle, RMS shown in top row and Correlation Length shown in bottom row

https://doi.org/10.5194/egusphere-2026-5457
Preprint. Discussion started: 2 November 2026
© Author(s) 2026. CC BY 4.0 License.

3.3.5 Snow Surface Roughness

As shown in Figure 15, the solid and dashed lines represent thin- and thick-snow scenarios, respectively, rather than smooth- and rough-snow configurations used in previous sections; the smooth snow representation by RMS and l_c is shown in the left and middle subplots, and the rough snow representation is shown in the right subplot characterized by MSS using the GO_B surface model. Sensitivity analysis has demonstrated that snow surface roughness contributes a considerable amount of backscatter to the SWOT sensor, with both thin- and thick-snow scenarios exhibiting very similar total backscatter responses and the same magnitude of snow surface backscatter contribution to variations in snow surface roughness (Figure 15). The difference between the backscatter responses of the smooth and rough snow configurations shows that IEM parameters from the smooth snow configuration exhibit greater sensitivity to the snow-surface contribution than GO_B parameters from the rough snow. Based on Figure A6 in the appendix, the snow surface backscatter sensitivity is stronger at near-nadir 1-2° incidence angles compared to other angles.

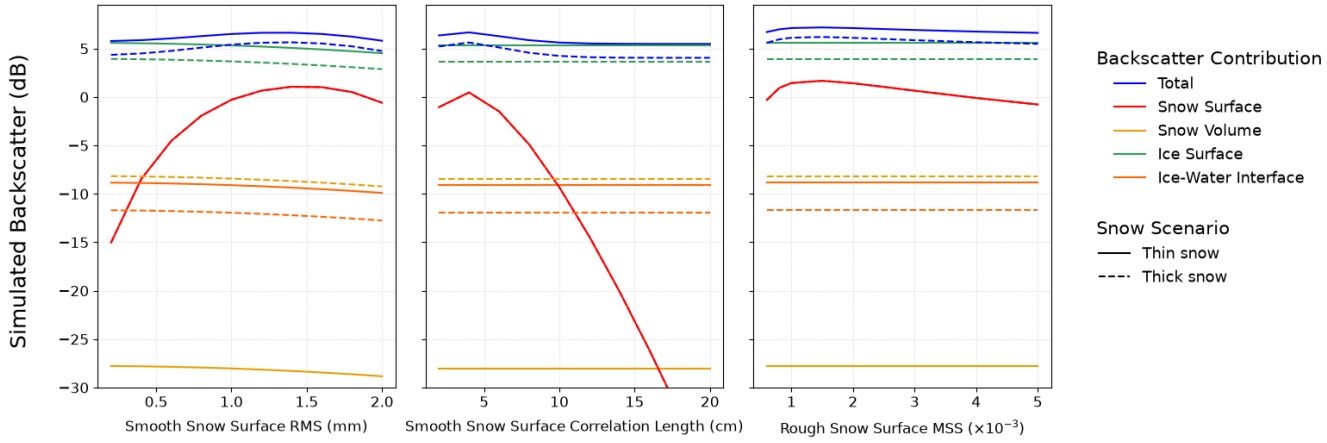


Figure 15. Snow surface roughness backscatter contribution at a fixed 3° incidence angle between thin and thick snow scenarios

3.3.6 Snow Density

The sensitivity analysis of snow density separates the influence into surface, volumetric, and basal snow components, followed by an assessment of the combined effect using bulk snow density (Figure 16). For surface snow density, the uppermost 0.5 cm of the snowpack was isolated, and its density was varied while the underlying snow layers and their microstructural properties were held constant at the baseline configuration. For basal snow density, the lowest 0.5 cm of snow immediately above the ice surface was isolated, and its density was varied while the properties of the overlying snowpack were held constant. For volumetric snow density, the surface and basal layers were held constant, while the density of the remaining snowpack varied to isolate the density response within the snow volume. The results show

https://doi.org/10.5194/egusphere-2026-5457
Preprint. Discussion started: 2 November 2026
© Author(s) 2026. CC BY 4.0 License.

contrasting responses depending on the snowpack location of the density change. Increasing surface snow density increases backscatter, whereas increasing basal snow density decreases backscatter in both thin and thick snow scenarios. Changes in volumetric snow density also decrease backscatter. Although the magnitude of the response is limited in the thin snow scenario, the volumetric response of snow density in the thick snow scenario is increased, but it remains weaker than the responses of surface and basal snow density. The layer-resolved results provide further insight into these contrasting density responses in Figure 17. Where increasing bulk density generally produces an increase in the snow-surface contribution and a corresponding decrease in the ice-surface contribution, while the snow-volume contribution remains relatively limited across the tested density range.

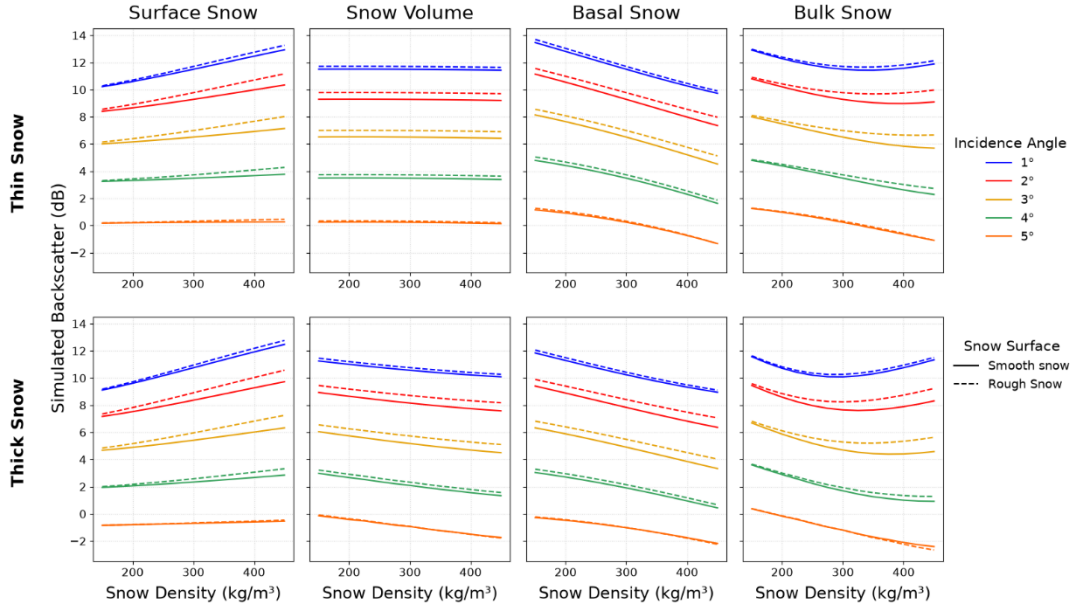


Figure 16. Sensitivity analysis of simulated backscatter to snow surface, volumetric, basal and bulk density under thin- and thick-snow conditions.

https://doi.org/10.5194/egusphere-2026-5457
Preprint. Discussion started: 2 November 2026
© Author(s) 2026. CC BY 4.0 License.

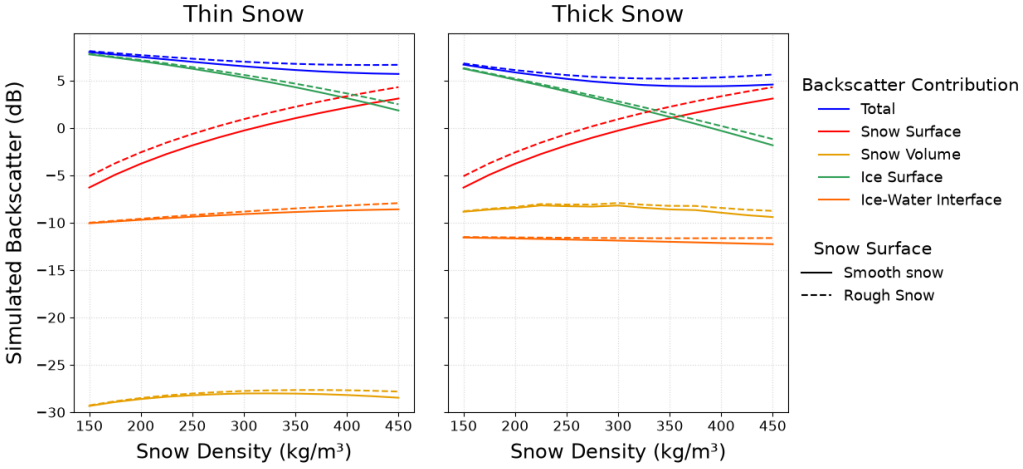


Figure 17. Backscatter contribution of snow bulk density at fixed 3° incidence angle under thick and thin snow scenarios

3.3.7 Snow Grain Size

The sensitivity analysis in Figure 18 shows a strong dependence of Ka-band backscatter on snow grain size under thick-snow conditions, while the response magnitude is negligible for thin snow. Here, ϕ is a scaling factor applied to the baseline parameter of the snow exponential correlation length, l_{ex}, and therefore reflects changes in the effective snow grain size. Based on the multiplication of ϕ and the baseline parameterization of l_{ex} in Table 4, the wind slab l_{ex} ranges from 0.03 to 0.12 mm, the faceted slab l_{ex} ranges from 0.075 to 0.3 mm, and the depth hoar l_{ex} ranges from 0.115 to 0.46 mm after ϕ is applied. Under thin-snow conditions, simulated backscatter remains nearly constant across the investigated range of ϕ, indicating limited sensitivity to grain size when the snowpack is shallow and the wind slab is the only snow layer. In contrast, under thick-snow and snow metamorphism conditions, increasing ϕ produces a pronounced decrease in backscatter. Also, the impact of snow grain size on surface snow was analyzed by applying ϕ to l_{ex} at the top 0.5 cm of the snowpack, where ϕ was stretched from 1 to 7 (similar to the depth hoar l_{ex} value when $\phi = 2$ is applied) due to the smaller grain size at the wind slab layer. As shown in Figure 19, the impact of snow grain size on surface snow backscatter was limited. Backscatter contributions across different layers further clarify the sensitivity of backscatter to snow grain size (Figure 19). In a thick snow scenario, when the grain size scaling factor ϕ increased, backscatter contribution from snow increased and backscatter from the ice surface decreased, while backscatter from the ice-water interface also decreased, thereby lowering overall backscatter. Interestingly, in the thin snow scenario, an increase in the scaling factor led to a considerable increase in snow-volume backscatter, while decreases in total and ice-surface backscatter were limited.

https://doi.org/10.5194/egusphere-2026-5457
Preprint. Discussion started: 2 November 2026
© Author(s) 2026. CC BY 4.0 License.

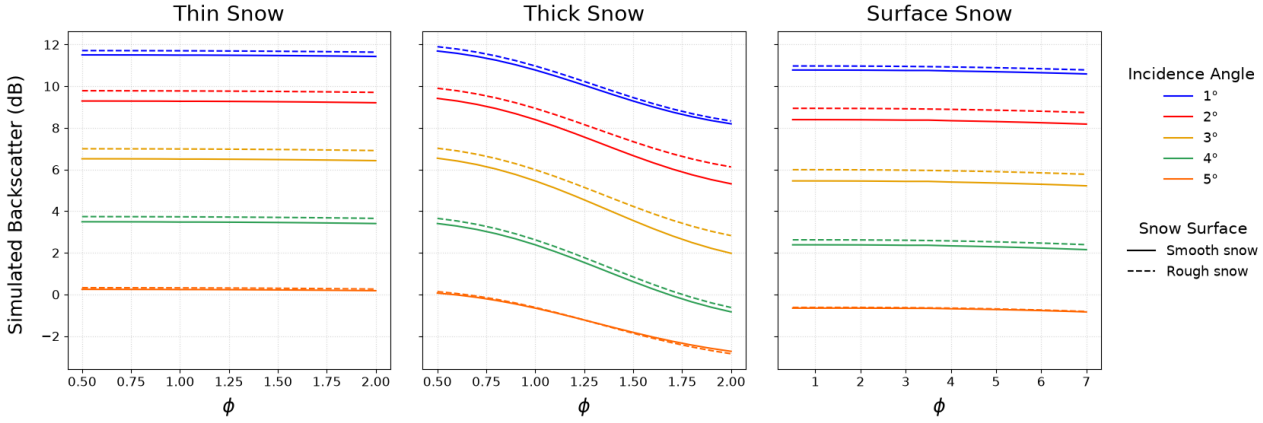


Figure 18. Sensitivity analysis of snow grain size, characterized by a scaling factor ϕ applied to exponential correlation length l_{ex}

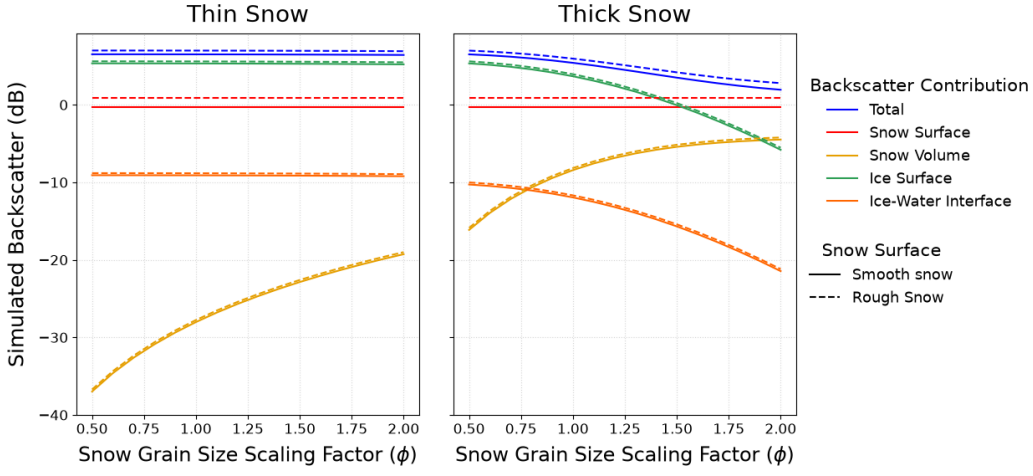


Figure 19. Backscatter contribution of snow grain size using a scaling factor ϕ, at fixed 3° incidence angle under thick and thin snow scenarios

4. Discussion

4.1 Backscatter mechanism of SWOT KaRIn on snow-covered lake ice

4.1.1 Ice Surface and Snow Surface

The NPC and sensitivity analyses based on SMRT simulation consistently identify ice-surface roughness as the strongest control on SWOT KaRIn backscatter under both smooth- and rough-snow conditions on Kluane Lake (Table 8; Figure 14). Together with the strong angular dependence, with backscatter decreasing from approximately 12 – 15 dB at 0.1° to −1 – 2

https://doi.org/10.5194/egusphere-2026-5457
Preprint. Discussion started: 2 November 2026
© Author(s) 2026. CC BY 4.0 License.

dB at 5° (Figure 7), these results provide supporting evidence that SWOT KaRIn observations over snow-covered ice are primarily characterized by quasi-specular surface scattering at the ice surface (Kacimi et al., 2025). However, the layer-resolved results further show that the dominant scattering characteristic does not always occur at the ice surface, but depends on the incidence angle and snow properties. For example, at near-nadir angles (0.1° - 1°), where the snow-surface contribution is only slightly lower than the ice-surface contribution for the thin-snow scenario and becomes nearly comparable for thick snow, whereas the ice surface becomes dominant at larger incidence angles, where snow-surface backscatter contribution decays faster than the ice surface. These characteristics demonstrate the ice-surface dominating the backscatter returns do not necessarily contradict previous Ka-band studies that report snow-surface-dominated returns over snow-covered sea ice and ice sheets (Laure et al., 2021; Rodríguez-Morales et al., 2021; Meloche et al., 2026), because those studies considered different snow depths and surface conditions, and under an altimetric nadir angle where a snow surface-dominant return is expected based on our layer-resolved analysis between backscatter and incidence angle. For example, the much thicker snowpacks on ice sheets up to 8 m in depth observed from Larue et al. (2021) and Rodríguez-Morales et al. (2021) would substantially attenuate the signal prior to interacting with the underlying ice-surface contribution, consistent with the decrease in ice-surface backscatter with increasing snow depth observed in this study. Similarly, observations reported by Meloche et al. (2026) and Stroeve et al. (2026) on sea ice have stronger snow-surface returns, primarily due to a rougher multi-year ice surface or salinity at the basal layer of snow on first-year ice modifies the relative scattering contributions. On the other hand, ground-based radar observations in Resolute Lake and Malcom Ramsay Lake also support this study's finding, where the dominant scattering interface of Ka-band radar on freshwater is the ice surface or snow-ice interface (Stroeve et al., 2026). Furthermore, recent radar altimetric sea-ice studies have also indicated a complex interaction between the snow and ice surfaces at both first-year and multi-year ice, in which radar echoes in the Ku and Ka bands do not originate primarily at the snow-ice interface but rather between the two (Landy et al., 2026; Taelman et al., 2026). Luo et al. (2026) compared SWOT-derived water surface elevation and elevation measurements from ICESat-2 representing snow surface heights, and found a considerable difference where elevation from ICESat-2 is higher than elevation from SWOT KaRIn during the winter period, providing further indication that the snow-ice interface is the dominant source of backscatter from SWOT. Thus, the apparent dominance of either the snow or ice surface is likely controlled by the combined effects of ice/snow surface roughness, snow properties, and incidence angle, rather than by a single universally dominant scattering centre.

Snow-surface roughness provides an additional control on the relative importance of snow surface scattering. The sensitivity experiments show that snow-surface roughness can substantially affect total backscatter (Figure 15). For the smooth-snow configuration, the RMS roughness produces a maximum response at approximately 1–1.5 mm, while the l_c has a relatively stable effect between approximately 2 and 6 cm, followed by a pronounced decrease in the snow-surface contribution when l_c exceeds approximately 6 cm (Figure 15). This abrupt decrease may reflect limitations of the IIEM formulation at larger l_c or indicate that l_c beyond 6 cm is no longer representative of the radar-scale roughness of the smooth snow surface. The smooth-snow roughness parameters adopted here are based on the in-situ measurements of Carletti et al.

https://doi.org/10.5194/egusphere-2026-5457
Preprint. Discussion started: 2 November 2026
© Author(s) 2026. CC BY 4.0 License.

(2025) using digital photography (Barella et al., 2026), whose observations showed dry-snow l_c remained below approximately 6 cm throughout the entire dry-snow period, supporting the applicability of the parameter range used in this study. In contrast, the GO_B formulation used for rough snow produces a substantially more stable response to l_c and RMS, consistent with its representation of larger-scale surface roughness rather than radar-scale microtopography. However, the snow surface contribution based on current results is only based on dry snow and ice conditions, where correct snow surface characterization during melting conditions needs further investigation and modelling. Footprint-scale roughness characterization on rough snow will also need to be further investigated for future study, although Gaussian autocorrelation have been demonstrated its robustness on rough snow surface (Larue et al., 2021), several current studies have concluded it might be more appropriate to adopt lognormal distribution footprint-scale roughness instead of gaussian distribution given that snow sastrugi can be characterized by as a combination of a predominantly smooth snow surface and occasional snow surface protrusions (Landy et al., 2019; Landy et al., 2020). However, the lognormal distribution is currently not widely implemented in SMRT, with the exception of the most recent implementation in SAR altimetry (Picard et al., 2026).

4.1.2 Snow depth and snow microstructure

While the ice-surface interaction is the primary contributor in most simulated SWOT KaRIn observations on snow-covered lake ice, snow depth and snow microstructure affect backscatter magnitude through attenuation. As shown in Figure 8, Figure 9, Figure 18, and Figure 19, increasing snow depth continually reduces the ice-surface contribution and consequently decreases total backscatter when the ice surface remains the dominant scattering mechanism. This attenuation is further enhanced by larger snow grains, indicating that snow microstructure governs the attenuation of the underlying ice-surface return. In contrast, snow-volume scattering increases with both snow depth and grain size, but approaches a saturation level of approximately −5 dB, beyond which additional increases in snow depth produce little change. This increase and eventual stabilization of snow-volume scattering with increasing snow depth is consistent with previous microwave snow theory, which shows that volume scattering increases until the snowpack becomes electromagnetically semi-infinite (Ulaby and Stiles, 1981). A similar saturation behaviour is observed in total backscatter for the three-layer snowpack with larger grain sizes (ϕ = 1.5 and 2), where the decrease in total backscatter becomes less pronounced beyond approximately 30 cm snow depth (Figures 8 and 9). The layer-resolved results indicate that this transition occurs when the ice-surface contribution has been sufficiently attenuated to become comparable to, and eventually lower than, the snow-surface and snow-volume contributions, causing further increases in snow depth starting to converge the backscatter decay.

4.1.3 Ice thickness and ice-water interfaces

Increasing ice thickness produces a decrease in simulated backscatter but has a relatively small effect on total backscatter (Figure 10). The layer-resolved results in Figure 11 indicate that this response is primarily associated with attenuation of the ice–water interface contribution as electromagnetic energy propagates through the ice column, with

https://doi.org/10.5194/egusphere-2026-5457
Preprint. Discussion started: 2 November 2026
© Author(s) 2026. CC BY 4.0 License.

dielectric loss progressively reducing the signal reaching and returning from the interface. This type of ice-thickness interaction has also been observed in Ku-band radar altimetry studies, with a negative association between ice thickness and backscatter (Zakharova et al., 2021; Li et al., 2022). The low sensitivity of ice–water interface roughness identified by the NPC analysis for 1.1 m ice thickness (Table 8) therefore reflects the already weak magnitude of the interface return rather than an intrinsically low sensitivity to roughness. This is demonstrated by Figure 12 and Figure 13, where the thinner 0.1 m ice configuration produces a substantially stronger ice–water interface contribution and correspondingly greater sensitivity of total backscatter to interface roughness. Interestingly, the presence of a thin snow layer further increases the sensitivity to the ice–water interface relative to bare ice, as the layer-resolved results in Figure 11 show a stronger overall interface contribution under thin-snow conditions. This can be attributed to the lower dielectric contrast at the snow–ice interface compared with the air–ice interface, which reduces the Fresnel reflection at the upper ice boundary and allows a greater fraction of the incident electromagnetic energy to penetrate into the ice and interact with the ice–water interface (Hallikainen et al., 1986).

4.1.3 Snow Density by Stratigraphy

The SWOT KaRIn backscatter sensitivity analysis shows that surface and basal snow density exert stronger controls on backscatter than volumetric snow density (Figure 16). Increasing surface snow density increases backscatter, with the response being more pronounced at lower incidence angles, consistent with the stronger contribution of the snow surface under near-nadir angle discussed in Section 4.1.1. In contrast, increasing basal snow density decreases backscatter consistently across the 1°–5° incidence-angle range. The opposing effects of surface and basal density produce a more pronounced U-shaped sensitivity of bulk density at lower incidence angles, which transitions toward a more linear decrease at higher incidence angles. The layer-resolved results further support this interpretation, showing that increasing bulk density primarily increases the snow-surface contribution and decreases the ice-surface contribution, while the snow-volume contribution remains relatively limited (Figure 17). Interestingly, the snow-volume backscatter contribution varies with snow density and illustrates a curve-like pattern, similar to the pattern of snow density from PM sensors (Welch and Kelly, 2025). These results suggest that the backscatter response to snow density is governed primarily by changes at the snow-air and snow-ice interfaces rather than by scattering from snow volume. Changes in snow density modify the effective relative permittivity of the snow, thereby altering the Fresnel reflection and transmission coefficients at the snow–air and snow–ice interfaces (Hallikainen et al., 1986). These findings are consistent with Larue et al. (2021), in which snow surface scattering dominates the volume scattering of snow at nadir incidence angles.

4.1.4 SWOT KaRIn Backscatter Time Series

Time-series observations from Mugunthan et al. (2026) provide observational support for the simulated scattering behaviour identified in this study. Their analysis of SWOT KaRIn backscatter over lake ice showed a gradual decrease in

https://doi.org/10.5194/egusphere-2026-5457
Preprint. Discussion started: 2 November 2026
© Author(s) 2026. CC BY 4.0 License.

backscatter prior to the onset of melting. Based on our sensitivity results, this decrease may reflect two concurrent processes: increasing lake-ice thickness, which reduces backscatter through greater attenuation within the ice column, and snowpack accumulation and metamorphism, where increasing snow depth and the development of larger grains, particularly depth hoar, progressively attenuate the signal reaching the snow–ice and ice–water interfaces. In contrast, the time series reported by Trudel et al. (2024) did not exhibit the same clear decreasing trend, which may be related to the absence of snow cover at their study lakes and potential surface melting during the observation period, where temporal change of snow properties does not exist. These comparisons suggest that the temporal evolution of SWOT KaRIn backscatter over lake ice can reflect changes in both ice thickness and snowpack evolution, rather than ice growth alone.

4.2 Current Limitations

SMRT simulations in Section 3.1. capture the dominant scattering behaviour observed by SWOT KaRIn, with overall RMSE values of 1.14 dB for smooth snow and 1.08 dB for rough snow, and a correlation coefficient of approximately 0.95 for both configurations. However, the model shows limited ability to reproduce the observed variability associated with snow water equivalent (SWE). Even among snow-pit sites with similar incidence angles, differences in backscatter could not be consistently distinguished according to SWE. This limitation is likely related to the lack of backscatter sensitivity to snow depth during the field campaign, due to the smaller snow grain size we observed, which differs from that reported in tundra studies. Future validation with field campaigns containing larger snow grain sizes would therefore provide an important test of the modelled snow-volume scattering and attenuation. Improved characterization of snow microstructure, including measurements of specific surface area (SSA) and in-situ instruments such as snow micropenetrometer (SMP), Photonic sensor, and InfraRed devices (IRIS), could further enhance the representation of spatially variable snow properties (Montpetit et al., 2024). Snow density also remains a source of uncertainty. Although vertical density profiles were measured within the snow pits, these measurements do not characterize the spatial variability of bulk density across the 100-meter SWOT raster product footprint. Moreover, the sensitivity analysis indicates that a substantial component of the density response originates from the snow surface, where snow density can change rapidly in response to wind redistribution and individual snowfall events, thereby introducing additional uncertainty between field measurements and conditions during the SWOT acquisition.

Another limitation is the assumption that snow-surface and ice-surface roughness is spatially consistent across all sampling sites. Assuming a consistent ice roughness level is based on visual interpretation during the field campaign where no snow ice layer was observed, which will introduce additional surface roughness. However, subtle differences in ice surface roughness among sites likely persist. This is particularly important because the sensitivity analysis demonstrates that even relatively small changes in RMS roughness can produce substantial changes in simulated backscatter. Consequently, some of the spatial variability in the observed SWOT backscatter may reflect unaccounted variability in ice-surface roughness rather than differences in snow properties or ice thickness alone. Although the snow surface roughness in the

https://doi.org/10.5194/egusphere-2026-5457
Preprint. Discussion started: 2 November 2026
© Author(s) 2026. CC BY 4.0 License.

smooth snow scenario can be assumed to be identical across sampling sites, the spatial variability of snow sastrugi in the rough snow scenario can introduce uncertainty. Future field campaigns should therefore include quantitative measurements of snow and ice surface roughness, such as chain measurements, digital photography, or structure-from-motion photogrammetry, to characterize both RMS roughness and its spatial correlation length (Meloche et al., 2021; Gunn et al., 2021). Such measurements would enable the incorporation of site-specific roughness parameters into SMRT, providing a more robust assessment of the contribution of surface roughness to SWOT Ka-band backscatter.

While the above uncertainties primarily concern differences among sampling sites within an acquisition and focus on limitations in our SMRT inputs, uncertainty also exists between SWOT acquisitions that comes from the SWOT KaRIn sensor. As shown in Table 5, most acquisitions exhibit correlations greater than 0.6 among the snow pit sites, whereas the D01 and E01 acquisitions show lower correlations of approximately 0.4. This is due to the difference in incidence angle: D01 and E01 acquisitions were observed at near-nadir incidence angles (0.43° - 1.42°), whereas other acquisitions were observed at far-nadir (3° - 4.38°). SWOT pixels at near-nadir geometry produce a coarser effective spatial resolution in the Pixel Cloud product, resulting in fewer point clouds available for aggregation into the raster product. Although raster aggregation generally reduces speckle noise by averaging multiple pixel-cloud observations, the smaller number of observations available under the near-nadir geometry may provide less effective noise reduction, leaving greater residual variability in the raster backscatter.

5. Conclusion

This study provides a modelling framework for improving the interpretation and potential for future retrieval of lake-ice and snow properties from SWOT KaRIn observations. Using SMRT, we demonstrate that backscatter from snow-covered lake ice is primarily controlled by scattering at the ice surface, while variations in sensor geometry and snow and ice properties can modify the relative contributions of surface and volume scattering. The comparison between modelled and observed backscatter obtained RMSEs of 1.14 dB for the smooth-snow configuration and 1.08 dB for the rough-snow configuration, and correlation coefficients of approximately 0.95. The application of the iterative second-order solver further enables quantitative separation of the contributions from the snowpack and ice interfaces, providing a basis for interpreting observed backscatter variations in terms of specific scattering mechanisms.

Overall, SMRT simulations identify the ice surface as the dominant scattering mechanism for SWOT KaRIn over snow-covered lake ice, although the relative importance of snow-surface and snow-volume scattering can increase with changes in SWOT viewing geometry and snow properties. The implementation of the second-order iterative solver in SMRT further enabled quantitative separation of backscatter contributions from individual snow and ice layers, providing a useful framework for interpreting the physical origin of observed Ka-band signals. These findings demonstrate the potential of combining SWOT interferometric height and backscatter to develop retrievals of lake-ice freeboard and overlying snow depth, while the temporal sensitivity of backscatter to snow conditions may provide additional information for monitoring

https://doi.org/10.5194/egusphere-2026-5457
Preprint. Discussion started: 2 November 2026
© Author(s) 2026. CC BY 4.0 License.

snow evolution when ice-surface roughness remains relatively stable. Specifically, the backscatter information provides a potential pathway for monitoring differential information in snow properties; although ice-surface roughness remains the dominant control on backscatter, its contribution may remain relatively stable throughout the frozen season in the absence of surface melt or ice surface overflow. Under such conditions, temporal changes in SWOT backscatter could primarily reflect changes in snowpack properties, including snow depth, density, and microstructure. Consequently, combining the temporal evolution of SWOT backscatter with interferometric height observations may provide a new approach for monitoring snow accumulation and metamorphism on lake ice and for developing integrated lake-ice and snow-property retrieval algorithms, particularly as SWOT observations are expected to continue beyond the current mission period.

Beyond lake ice, the modelling framework developed in this study can also serve as a prototype for investigating SWOT KaRIn observations over sea ice. Several recent studies have provided initial assessments of SWOT's capability to observe sea-ice freeboard (Kacimi et al., 2025; Müller et al., 2026); however, the interaction of Ka-band radar with the snowpack and the resulting penetration effects remain important sources of uncertainty in sea-ice freeboard retrieval (Landy et al., 2026). The freshwater-ice framework established here provides a physically based starting point for extending SMRT simulations to snow-covered sea ice, where appropriate modifications to the snow and ice dielectric properties, snow stratigraphy, and interface conditions can be incorporated. Such an extension could improve understanding of KaRIn–snow–ice interactions and help quantify the effects of snow penetration and scattering-horizon variability on SWOT sea-ice freeboard measurements.

The SWOT KaRIn modelling framework presented here could also be transferable to future Ka-band missions and applications. For example, the upcoming Copernicus Polar Ice and Snow Topography Altimeter (CRISTAL) mission will provide dual-frequency Ku- and Ka-band radar observations designed to improve the characterization of snow and ice properties (Kern et al., 2020), while conceptual missions such as DLR's Synthetic Aperture Radar for Glacier and global Dynamics (SIGNAL) envision Ka-band interferometric observations of snow and ice surfaces (Börner et al., 2010). These results also provide important information for improving radar altimetry measurements of lake-ice thickness, because snow penetration and volume scattering can shift the effective radar scattering horizon and introduce uncertainty into ice-thickness retrievals (Mangilli et al., 2024). Integrating the physical understanding developed here with interferometric height and backscatter observations could therefore enable next-generation retrieval approaches for snow-covered lakes and sea ice. More broadly, the results provide a prototype for interpreting future Ka-band satellite observations and can help guide the design of retrieval algorithms and targeted field campaigns needed to establish robust long-term records of snow and ice properties.

https://doi.org/10.5194/egusphere-2026-5457
Preprint. Discussion started: 2 November 2026
© Author(s) 2026. CC BY 4.0 License.

Appendix A

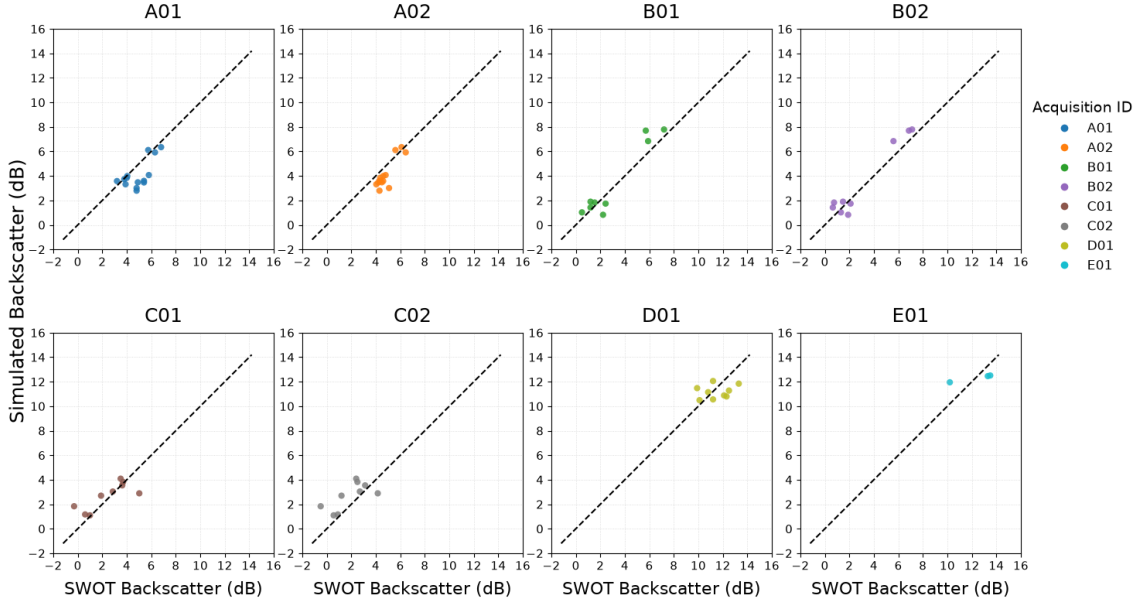


Figure A1. Comparison of SWOT-observed and SMRT-simulated backscatter using optimized ice roughness parameters (RMS = 1.25mm, l_c = 5cm) for individual acquisitions in the rough snow scenarios (GO_B)

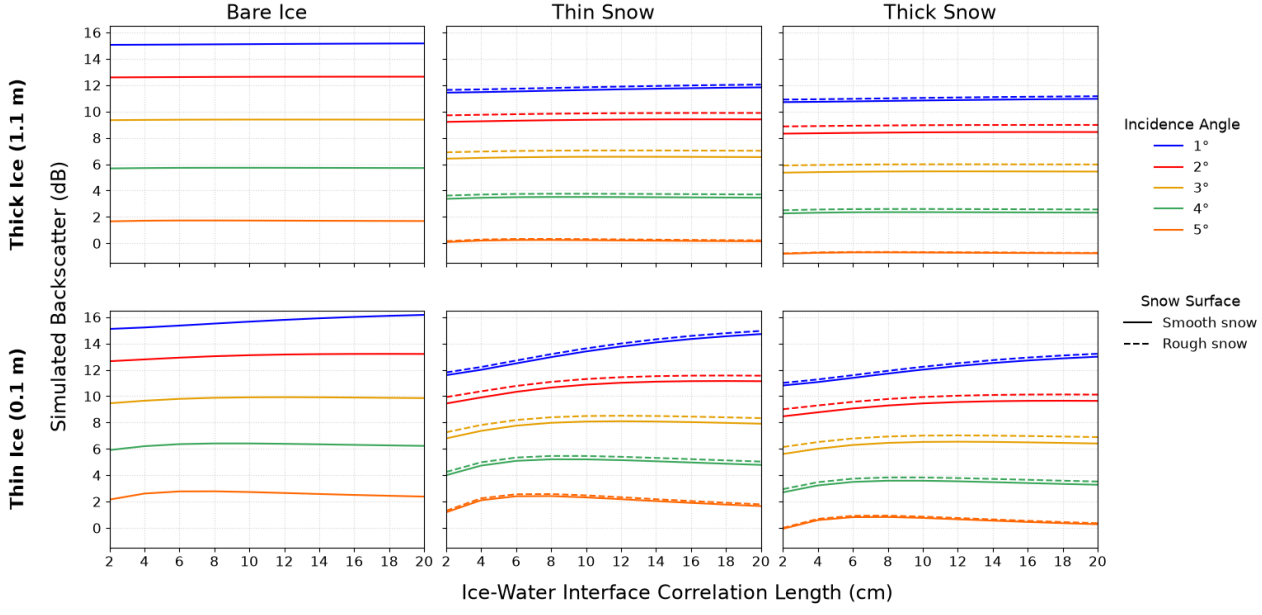


Figure A2. Sensitivity analysis of the ice-water interface l_c at different snow scenarios and incidence angle, with comparison between thick (1.1 m ice thickness) and thin ice (0.1 m ice thickness).

https://doi.org/10.5194/egusphere-2026-5457
Preprint. Discussion started: 2 November 2026
© Author(s) 2026. CC BY 4.0 License.



780

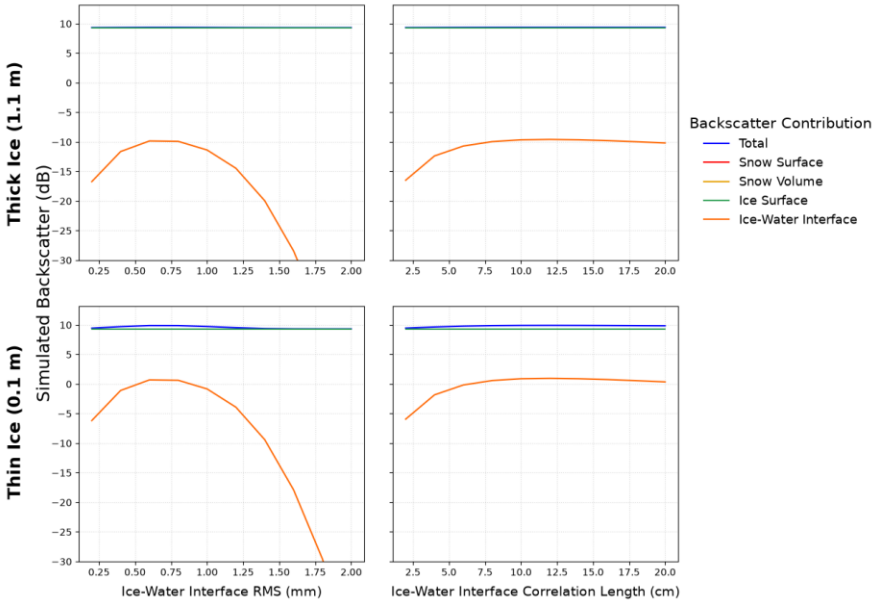
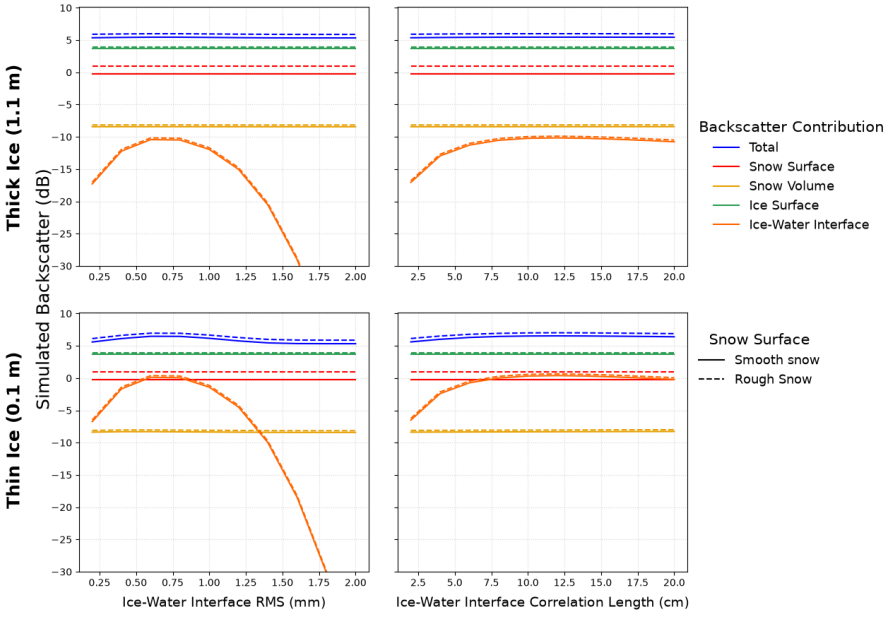


Figure A3. Backscatter contribution from the ice-water interface roughness at a fixed 3° incidence angle and bare ice condition, varied with different ice thicknesses



785

Figure A4. Backscatter contribution from Ice-Water interface roughness at a fixed 3° incidence angle and thick snow conditions, varied with different ice thicknesses

https://doi.org/10.5194/egusphere-2026-5457
Preprint. Discussion started: 2 November 2026
© Author(s) 2026. CC BY 4.0 License.

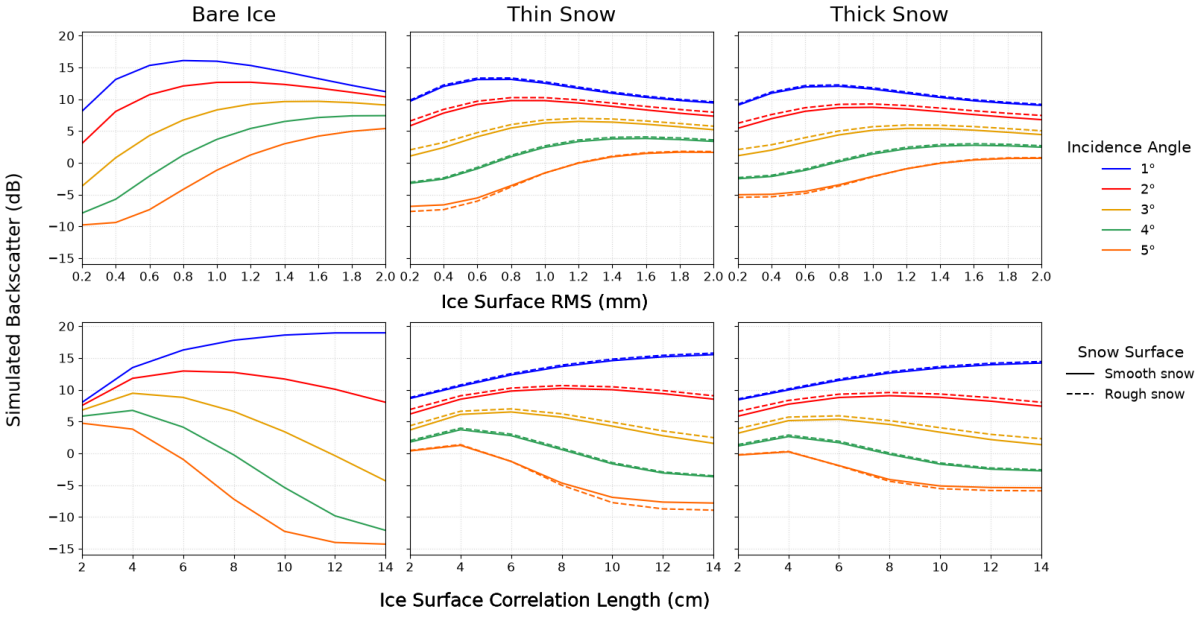


Figure A5. Backscatter sensitivity of Ice surface roughness properties at varied snow cover scenarios and incidence angle, RMS shown in the top row and l_c shown in the bottom row.

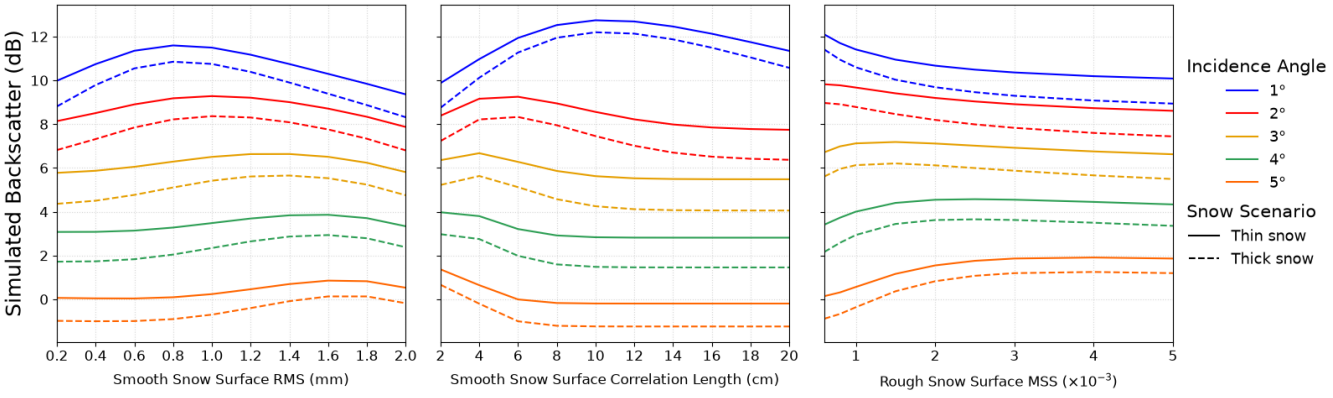


Figure A6. Sensitivity of simulated backscatter to different snow-surface roughness parameters with varying SWOT incidence angle under thin- and thick-snow conditions.

https://doi.org/10.5194/egusphere-2026-5457
Preprint. Discussion started: 2 November 2026
© Author(s) 2026. CC BY 4.0 License.

Code and data availability.

SMRT simulated records, codes for generating plots/graphs, and the SMRT framework for this study are available at 10.5281/zenodo.22289519. SWOT data are publicly available from doi.org/10.5067/SWOT-RASTER-D. SMRT model code is available on GitHub: github.com/smrt-model/smrt (v 1.6). Others can be obtained upon request from the corresponding author.

Author contributions

G.G. conceptualized the study, P.C. and G.G. completed the data curation, P.C. completed the formal analysis (statistical testing, modifying simulations), P.C. conducted the investigation with G.G.; and P.C. contributed to the methodology. J.M. implemented the second-order iterative solver in SMRT. Funding acquisition, resources and supervision were provided by G.G. Validation and visualizations were completed by P.C. Writing of the original draft was completed by P.C., with reviewing and editing provided by P.C., J.M., and G.G.

Competing interests

The contact author has declared that neither of the authors has any competing interests.

Disclaimer

Copernicus Publications remains neutral with regard to jurisdictional claims made in the text, published maps, institutional affiliations, or any other geographical representation in this paper. While Copernicus Publications makes every effort to include appropriate place names, the final responsibility lies with the authors. Views expressed in the text are those of the authors and do not necessarily reflect the views of the publisher.

Acknowledgements

The authors would like to thank Hayley Kavanagh, Sukhdip Kharoud, and Sam White for their help in field data collection on Lhù'àän Mân (Kluane Lake) during March 2026. Thank you to Dr. Richard Kelly for early-stage advice and suggestions for this study. A profound thank you to Dr. Melody Sandells for guidance in SMRT model configuration and design. We acknowledge that this research was conducted in the traditional territory of the Kluane Lake First Nation and respectfully recognize their connection to and stewardship of the land and waters of the region.

https://doi.org/10.5194/egusphere-2026-5457
Preprint. Discussion started: 2 November 2026
© Author(s) 2026. CC BY 4.0 License.

Financial support

This research was funded by the Canadian Space Agency through the Research Opportunities in Space Science (ROSS) 23SUESLAKE for student support during research and analysis, and Dr. Gunn's Natural Sciences and Engineering Research Council of Canada Discovery Grant (RGPIN-2021-02742) for travel and field data collection.

Review statement

The review statement will be added by Copernicus Publications listing the handling editor as well as all contributing referees according to their status anonymous or identified.

https://doi.org/10.5194/egusphere-2026-5457
Preprint. Discussion started: 2 November 2026
© Author(s) 2026. CC BY 4.0 License.

References

Bacal, N. G. and Brown, L. C.: The underside of the ice: Exploring the relationship between ice thickness and the roughness of the ice-water interface for freshwater lakes in Central Ontario, Cold Regions Science and Technology, 247, 104910, https://doi.org/10.1016/j.coldregions.2026.104910, 2026.

Barella, R., Carletti, F., Scheidt, K. T., Mazza, A., Bavay, M., Walter, B., and Marin, C.: Characterizing snow roughness: A novel low-cost portable tool based on ChArUco board and digital photography, Cold Regions Science and Technology, 251, 105013, https://doi.org/10.1016/j.coldregions.2026.105013, 2026.

Belinska, K., Fischer, G., and Hajnsek, I.: Combining Differential SAR Interferometry and Copolar Phase Differences for Snow Water Equivalent Estimation, IEEE Geosci. Remote Sensing Lett., 21, 1–5, https://doi.org/10.1109/LGRS.2024.3461229, 2024.

Börner, T., De Zan, F., López-Dekker, P., Krieger, G., Hajnsek, I., Papathanassiou, K., Villano, M., Younis, M., Danklmayer, A., Dierking, W., Nagler, T., Rott, H., Lehner, S., Fügen, T., and Moreira, A.: SIGNAL: SAR for ice, glacier and global dynamics. In 2010 IEEE International Geoscience and Remote Sensing Symposium, 2884-2887, 10.1109/IGARSS.2010.5653162, 2010.

Brahney, J., Clague, J. J., Menounos, B., and Edwards, T., W. D.: Timing and cause of water level fluctuations in Kluane Lake, Yukon Territory, over the past 5000 years, Quat. res., 70, 213–227, https://doi.org/10.1016/j.yqres.2008.05.001, 2008.

Brogioni, M., Pettinato, S., Macelloni, G., Paloscia, S., Pampaloni, P., Pierdicca, N., and Ticconi, F.: Sensitivity of bistatic scattering to soil moisture and surface roughness of bare soils, International Journal of Remote Sensing, 31, 4227–4255, https://doi.org/10.1080/01431160903232808, 2010.

Brown, L. C. and Duguay, C. R.: The response and role of ice cover in lake-climate interactions, Progress in Physical Geography: Earth and Environment, 34, 671–704, https://doi.org/10.1177/0309133310375653, 2010.

Carletti, F., Marin, C., Ghielmini, C., Bavay, M., and Lehning, M.: Multitemporal analysis of Sentinel-1 backscatter during snowmelt using high-resolution field measurements and radiative transfer modelling, The Cryosphere, 19, 5579–5612, https://doi.org/10.5194/tc-19-5579-2025, 2025.

Clifford, D.: Global estimates of snow water equivalent from passive microwave instruments: history, challenges and future developments, International Journal of Remote Sensing, 31, 3707–3726, https://doi.org/10.1080/01431161.2010.483482, 2010.

https://doi.org/10.5194/egusphere-2026-5457
Preprint. Discussion started: 2 November 2026
© Author(s) 2026. CC BY 4.0 License.

Colbeck, S. C.: An overview of seasonal snow metamorphism, Reviews of Geophysics, 20, 45–61, https://doi.org/10.1029/RG020i001p00045, 1982.

De Rijke-Thomas, C., Landy, J. C., Mallett, R., Willatt, R. C., Tsamados, M., and King, J.: Airborne Investigation of Quasi-Specular Ku-Band Radar Scattering for Satellite Altimetry Over Snow-Covered Arctic Sea Ice, IEEE Trans. Geosci. Remote Sensing, 61, 1–19, https://doi.org/10.1109/TGRS.2023.3318263, 2023.

Derksen, C., Walker, A., and Goodison, B.: Evaluation of passive microwave snow water equivalent retrievals across the boreal forest/tundra transition of western Canada, Remote Sensing of Environment, 96, 315–327, https://doi.org/10.1016/j.rse.2005.02.014, 2005.

Durand, M., Kim, E. J., and Margulis, S. A.: Quantifying Uncertainty in Modeling Snow Microwave Radiance for a Mountain Snowpack at the Point-Scale, Including Stratigraphic Effects, IEEE Trans. Geosci. Remote Sensing, 46, 1753–1767, https://doi.org/10.1109/TGRS.2008.916221, 2008.

Environment and Climate Change Canada: Canadian Climate Normals 1981–2020 Station Data: Burwash Landing, Yukon, Government of Canada [data set], https://climate.weather.gc.ca/climate_normals/index_e.html, 2021.

Fan, Y., Li, L., Chen, H., and Guan, L.: Evaluation and Application of SMRT Model for L-Band Brightness Temperature Simulation in Arctic Sea Ice, Remote Sensing, 15, 3889, https://doi.org/10.3390/rs15153889, 2023.

Fierz, C., Armstrong, R. L., Durand, Y., Etchevers, P., Greene, E., McClung, D. M., Nishimura, K., Satyawali, P. K., and Sokratov, S. A.: The International Classification for Seasonal Snow on the Ground, IHP-VII Technical Documents in Hydrology No.83, IACS Contribution No.1, UNESCO-IHP, Paris, https://unesdoc.unesco.org/ark:/48223/pf0000186462 (last access: 10 August 2026), 2009.

Fjortoft, R., Gaudin, J.-M., Pourthie, N., Lalaurie, J.-C., Mallet, A., Nouvel, J.-F., Martinot-Lagarde, J., Oriot, H., Borderies, P., Ruiz, C., and Daniel, S.: KaRIn on SWOT: Characteristics of Near-Nadir Ka-Band Interferometric SAR Imagery, IEEE Trans. Geosci. Remote Sensing, 52, 2172–2185, https://doi.org/10.1109/TGRS.2013.2258402, 2014.

Foster, J. L., Sun, C., Walker, J. P., Kelly, R., Chang, A., Dong, J., and Powell, H.: Quantifying the uncertainty in passive microwave snow water equivalent observations, Remote Sensing of Environment, 94, 187–203, https://doi.org/10.1016/j.rse.2004.09.012, 2005.

Fu, L., Pavelsky, T., Cretaux, J., Morrow, R., Farrar, J. T., Vaze, P., Sengenes, P., Vinogradova-Shiffer, N., Sylvestre-Baron, A., Picot, N., and Dibarboure, G.: The Surface Water and Ocean Topography Mission: A Breakthrough in Radar Remote

https://doi.org/10.5194/egusphere-2026-5457
Preprint. Discussion started: 2 November 2026
© Author(s) 2026. CC BY 4.0 License.

Sensing of the Ocean and Land Surface Water, Geophysical Research Letters, 51, e2023GL107652, https://doi.org/10.1029/2023GL107652, 2024.

Fung, A. K. and Chen, K. S.: An Update on the IEM Surface Backscattering Model, IEEE Geosci. Remote Sensing Lett., 1, 75–77, https://doi.org/10.1109/LGRS.2004.826564, 2004.

Fung, A. K. and Chen, K.-S.: Microwave scattering and emission models for users, Artech House, Boston London, 1 p., 2010.

Fung, A. K., Liu, W. Y., Chen, K. S., and Tsay, M. K.: An Improved Iem Model for Bistatic Scattering From Rough Surfaces, Journal of Electromagnetic Waves and Applications, 16, 689–702, https://doi.org/10.1163/156939302X01119, 2002.

Gélinas, A., Montpetit, B., Meloche, J., Toose, P., Akhavan, Z., Wang, W., Kelly, R., Langlois, A., and Roy, A.: Soil microwave background retrieval and snow sensitivity from multi-frequency SAR observations over an agro-forested environment in northern Ontario, EGUsphere [preprint], https://doi.org/10.5194/egusphere-2026-656, 2026.

Gunn, G. E., Duguay, C. R., Derksen, C., Lemmetyinen, J., and Toose, P.: Evaluation of the HUT modified snow emission model over lake ice using airborne passive microwave measurements, Remote Sensing of Environment, 115, 233–244, https://doi.org/10.1016/j.rse.2010.09.001, 2011.

Gunn, G. E., Brogioni, M., Duguay, C., Macelloni, G., Kasurak, A., and King, J.: Observation and Modeling of X- and Ku-Band Backscatter of Snow-Covered Freshwater Lake Ice, IEEE J. Sel. Top. Appl. Earth Observations Remote Sensing, 8, 3629–3642, https://doi.org/10.1109/JSTARS.2015.2420411, 2015.

Gunn, G. E., Jones, B. M., and Rangel, R. C.: Unpiloted Aerial Vehicle Retrieval of Snow Depth Over Freshwater Lake Ice Using Structure From Motion, Front. Remote Sens., 2, 675846, https://doi.org/10.3389/frsen.2021.675846, 2021.

Hallikainen, M. T., Ulaby, F. T., and Abdelrazik, M.: Dielectric properties of snow in the 3 to 37 GHz range, IEEE Trans. Antennas Propag., 34, 1329–1340, https://doi.org/10.1109/TAP.1986.1143757, 1986.

Kacimi, S., Jaruwatanadilok, S., and Kwok, R.: SWOT Observations Over Sea Ice: A First Look, Geophysical Research Letters, 52, e2025GL116079, https://doi.org/10.1029/2025GL116079, 2025.

Karam, M. A., Amar, F., Fung, A. K., Mougin, E., Lopes, A., Le Vine, D. M., and Beaudoin, A.: A microwave polarimetric scattering model for forest canopies based on vector radiative transfer theory, Remote Sensing of Environment, 53, 16–30, https://doi.org/10.1016/0034-4257(95)00048-6, 1995.

https://doi.org/10.5194/egusphere-2026-5457
Preprint. Discussion started: 2 November 2026
© Author(s) 2026. CC BY 4.0 License.

Kelly, R. E., Chang, A. T., Tsang, L., and Foster, J. L.: A prototype AMSR-E global snow area and snow depth algorithm, IEEE Trans. Geosci. Remote Sensing, 41, 230–242, https://doi.org/10.1109/TGRS.2003.809118, 2003.

Kern, M., Cullen, R., Berruti, B., Bouffard, J., Casal, T., Drinkwater, M. R., Gabriele, A., Lecuyot, A., Ludwig, M., Midthassel, R., Navas Traver, I., Parrinello, T., Ressler, G., Andersson, E., Martin-Puig, C., Andersen, O., Bartsch, A., Farrell, S., Fleury, S., Gascoin, S., Guillot, A., Humbert, A., Rinne, E., Shepherd, A., van den Broeke, M. R., and Yackel, J.: The Copernicus Polar Ice and Snow Topography Altimeter (CRISTAL) high-priority candidate mission, The Cryosphere, 14, 2235–2251, https://doi.org/10.5194/tc-14-2235-2020, 2020.

King, J., Kelly, R., Kasurak, A., Duguay, C., Gunn, G., Rutter, N., Watts, T., and Derksen, C.: Spatio-temporal influence of tundra snow properties on Ku-band (17.2 GHz) backscatter, J. Glaciol., 61, 267–279, https://doi.org/10.3189/2015JoG14J020, 2015.

King, J., Derksen, C., Toose, P., Langlois, A., Larsen, C., Lemmetyinen, J., Marsh, P., Montpetit, B., Roy, A., Rutter, N., and Sturm, M.: The influence of snow microstructure on dual-frequency radar measurements in a tundra environment, Remote Sensing of Environment, 215, 242–254, https://doi.org/10.1016/j.rse.2018.05.028, 2018.

Landy, J. C., Tsamados, M., and Scharien, R. K.: A Facet-Based Numerical Model for Simulating SAR Altimeter Echoes From Heterogeneous Sea Ice Surfaces, IEEE Trans. Geosci. Remote Sensing, 57, 4164–4180, https://doi.org/10.1109/TGRS.2018.2889763, 2019.

Landy, J. C., Petty, A. A., Tsamados, M., and Stroeve, J. C.: Sea ice roughness overlooked as a key source of uncertainty in CryoSat-2 ice freeboard retrievals, *J. Geophys. Res.-Oceans*, 125, e2019JC015820, https://doi.org/10.1029/2019JC015820, 2020.

Landy, J. C., De Rijke-Thomas, C., Nab, C., Lawrence, I., Glissenaar, I. A., Mallett, R. D. C., Fredensborg Hansen, R. M., Petty, A., Tsamados, M., Macfarlane, A. R., and Braakmann-Folgmann, A.: Anticipating CRISTAL: an exploration of multi-frequency satellite altimeter snow depth estimates over Arctic sea ice, 2018–2023, The Cryosphere, 20, 183–208, https://doi.org/10.5194/tc-20-183-2026, 2026.

Larue, F., Picard, G., Aublanc, J., Arnaud, L., Robledano-Perez, A., Le Meur, E., Favier, V., Jourdain, B., Savarino, J., and Thibaut, P.: Radar altimeter waveform simulations in Antarctica with the Snow Microwave Radiative Transfer Model (SMRT), Remote Sensing of Environment, 263, 112534, https://doi.org/10.1016/j.rse.2021.112534, 2021.

Lemmetyinen, J., Derksen, C., Pulliainen, J., Strapp, W., Toose, P., Walker, A., Tauriainen, S., Pihlflyckt, J., Karna, J.-P., and Hallikainen, M. T.: A Comparison of Airborne Microwave Brightness Temperatures and Snowpack Properties Across

https://doi.org/10.5194/egusphere-2026-5457
Preprint. Discussion started: 2 November 2026
© Author(s) 2026. CC BY 4.0 License.

the Boreal Forests of Finland and Western Canada, IEEE Trans. Geosci. Remote Sensing, 47, 965–978, https://doi.org/10.1109/TGRS.2008.2006358, 2009.

Lemmetyinen, J., Pulliainen, J., Rees, A., Kontu, A., Qiu, Y., and Derksen, C.: Multiple-layer adaptation of HUT snow emission model: Comparison with experimental data, IEEE Trans. Geosci. Remote Sensing, 48, 2781–2794, https://doi.org/10.1109/TGRS.2009.2035765, 2010.

Lemmetyinen, J., Derksen, C., Rott, H., Macelloni, G., King, J., Schneebeli, M., Wiesmann, A., Leppänen, L., Kontu, A., and Pulliainen, J.: Retrieval of Effective Correlation Length and Snow Water Equivalent from Radar and Passive Microwave Measurements, Remote Sensing, 10, 170, https://doi.org/10.3390/rs10020170, 2018.

Li, X., Long, D., Cui, Y., Liu, T., Lu, J., Hamouda, M. A., and Mohamed, M. M.: Ice thickness and water level estimation for ice-covered lakes with satellite altimetry waveforms and backscattering coefficients, The Cryosphere, 17, 349–369, https://doi.org/10.5194/tc-17-349-2023, 2023.

Li, Q., Kelly, R., and Leppänen, L.: Land snow surface temperature estimation using an optimized near real-time passive microwave algorithm, IEEE Trans. Geosci. Remote Sens., 63, 1–12, https://doi.org/10.1109/TGRS.2025.3528333, 2025.

Lievens, H., Demuzere, M., Marshall, H.-P., Reichle, R. H., Brucker, L., Brangers, I., De Rosnay, P., Dumont, M., Girotto, M., Immerzeel, W. W., Jonas, T., Kim, E. J., Koch, I., Marty, C., Saloranta, T., Schöber, J., and De Lannoy, G. J. M.: Snow depth variability in the Northern Hemisphere mountains observed from space, Nat Commun, 10, 4629, https://doi.org/10.1038/s41467-019-12566-y, 2019.

Löwe, H. and Picard, G.: Microwave scattering coefficient of snow in MEMLS and DMRT-ML revisited: the relevance of sticky hard spheres and tomography-based estimates of stickiness, The Cryosphere, 9, 2101–2117, https://doi.org/10.5194/tc-9-2101-2015, 2015.

Luo, S., Song, C., Zhan, P., Li, J., and Peng, L.: A First Look at the Snow/Ice Penetration Effect of SWOT Observations on Water Level of Global Glacial Lakes, Geophysical Research Letters, 53, e2026GL122624, https://doi.org/10.1029/2026GL122624, 2026.

Luojus, K., Pulliainen, J., Takala, M., Lemmetyinen, J., Mortimer, C., Derksen, C., Mudryk, L., Moisander, M., Hiltunen, M., Smolander, T., Ikonen, J., Cohen, J., Salminen, M., Norberg, J., Veijola, K., and Venäläinen, P.: GlobSnow v3.0 Northern Hemisphere snow water equivalent dataset, Sci Data, 8, 163, https://doi.org/10.1038/s41597-021-00939-2, 2021.

https://doi.org/10.5194/egusphere-2026-5457
Preprint. Discussion started: 2 November 2026
© Author(s) 2026. CC BY 4.0 License.

Mangilli, A., Duguay, C. R., Murfitt, J., Moreau, T., Amraoui, S., Mugunthan, J. S., Thibaut, P. and Donlon, C.: Improving the estimation of lake ice thickness with high-resolution radar altimetry data, Remote Sens., 16, 2510, https://doi.org/10.3390/rs16142510, 2024.

Mätzler, C.: Improved Born approximation for scattering of radiation in a granular medium, Journal of Applied Physics, 83, 6111–6117, https://doi.org/10.1063/1.367496, 1998.

Mätzler, C.: Relation between grain-size and correlation length of snow, J. Glaciol., 48, 461–466, https://doi.org/10.3189/172756502781831287, 2002.

McKnight, E. A., Swanson, H., Brahney, J., and Hik, D. S.: The physical and chemical limnology of Yukon's largest lake, Lhù'ààn Mân' (Kluane Lake), prior to the 2016 'A'ą̈y Chù' diversion, Arctic Science, 7, 655–678, https://doi.org/10.1139/as-2020-0012, 2021.

Meloche, J., Royer, A., Langlois, A., Rutter, N., and Sasseville, V.: Improvement of microwave emissivity parameterization of frozen Arctic soils using roughness measurements derived from photogrammetry, International Journal of Digital Earth, 14, 1380–1396, https://doi.org/10.1080/17538947.2020.1836049, 2021.

Meloche, J., Sandells, M., Löwe, H., Rutter, N., Picard, G., Essery, R., Scharien, R. K., Langlois, A., Jaggi, M., King, J., Toose, P., Scagliola, M., Bouffard, J., Di Bella, A., and Haas, C.: Altimetric Ku-band Radar Observations of Snow on Sea Ice Simulated with SMRT, EGUsphere [preprint], https://doi.org/10.5194/egusphere-2026-3615, 2026.

Montpetit, B., King, J., Meloche, J., Derksen, C., Siqueira, P., Adam, J. M., Toose, P., Brady, M., Wendleder, A., Vionnet, V., and Leroux, N. R.: Retrieval of snow and soil properties for forward radiative transfer modeling of airborne Ku-band SAR to estimate snow water equivalent: the Trail Valley Creek 2018/19 snow experiment, The Cryosphere, 18, 3857–3874, https://doi.org/10.5194/tc-18-3857-2024, 2024.

Müller, F. L., Dettmering, D., and Seitz, F.: First arctic-wide assessment of SWOT swath altimetry with ICESat-2 over sea ice, The Cryosphere, 20, 397–409, https://doi.org/10.5194/tc-20-397-2026, 2026.

Mugunthan, J. S., Duguay, C. R., Murfitt, J., Zakharova, E., and Jones, B. M.: First Assessment of SWOT KaRIn Measurements Over Lake Ice and Overlying Snow, EGUsphere [preprint], https://doi.org/10.5194/egusphere-2026-4309, 2026.

© Author(s) 2026. CC BY 4.0 License.

Murfitt, J., Duguay, C. R., Picard, G., and Gunn, G. E.: Investigating the Effect of Lake Ice Properties on Multifrequency Backscatter Using the Snow Microwave Radiative Transfer Model, IEEE Trans. Geosci. Remote Sensing, 60, 1–23, https://doi.org/10.1109/TGRS.2022.3197109, 2022.

Murfitt, J., Duguay, C., Picard, G., and Gunn, G.: Forward modelling of synthetic aperture radar backscatter from lake ice over Canadian Subarctic Lakes, Remote Sensing of Environment, 286, 113424, https://doi.org/10.1016/j.rse.2022.113424, 2023.

Murfitt, J., Duguay, C., Picard, G., and Lemmetyinen, J.: Forward modelling of synthetic-aperture radar (SAR) backscatter during lake ice melt conditions using the Snow Microwave Radiative Transfer (SMRT) model, The Cryosphere, 18, 869–888, https://doi.org/10.5194/tc-18-869-2024, 2024.

Picard, G., Le Toan, T., Quegan, S., Caraglio, Y., and Castel, T.: Radiative transfer modeling of cross-polarized backscatter from a pine forest using the discrete ordinate and eigenvalue method, IEEE Trans. Geosci. Remote Sensing, 42, 1720–1730, https://doi.org/10.1109/TGRS.2004.831229, 2004.

Picard, G., Sandells, M., and Löwe, H.: SMRT: an active–passive microwave radiative transfer model for snow with multiple microstructure and scattering formulations (v1.0), Geosci. Model Dev., 11, 2763–2788, https://doi.org/10.5194/gmd-11-2763-2018, 2018.

Picard, G., Löwe, H., and Mätzler, C.: Brief communication: A continuous formulation of microwave scattering from fresh snow to bubbly ice from first principles, The Cryosphere, 16, 3861–3866, https://doi.org/10.5194/tc-16-3861-2022, 2022a.

Picard, G., Löwe, H., Domine, F., Arnaud, L., Larue, F., Favier, V., Le Meur, E., Lefebvre, E., Savarino, J., and Royer, A.: The Microwave Snow Grain Size: A New Concept to Predict Satellite Observations Over Snow-Covered Regions, AGU Advances, 3, e2021AV000630, https://doi.org/10.1029/2021AV000630, 2022b.

Picard, G., Murfitt, J., Zakharova, E., Zeiger, P., Arnaud, L., Aublanc, J., Landy, J. C., Scagliola, M., and Duguay, C.: Simulating SAR altimeter echoes from cryospheric surfaces with the Snow Microwave Radiative Transfer (SMRT) model version sarm-v0, EGUsphere [preprint], https://doi.org/10.5194/egusphere-2025-6056, 2026.

Pouw, A. F., Kheyrollah Pour, H., and MacLean, A.: Mapping snow depth on Canadian sub-arctic lakes using ground-penetrating radar, The Cryosphere, 17, 2367–2385, https://doi.org/10.5194/tc-17-2367-2023, 2023.

https://doi.org/10.5194/egusphere-2026-5457
Preprint. Discussion started: 2 November 2026
© Author(s) 2026. CC BY 4.0 License.

Rodríguez-Morales, F., et al.: A compact, reconfigurable, multi-UWB radar for snow thickness evaluation and altimetry: Development and field trials, IEEE J. Sel. Top. Appl. Earth Obs. Remote Sens., 14, 6755–6765, https://doi.org/10.1109/JSTARS.2021.3092313, 2021.

Rott, H., Yueh, S. H., Cline, D. W., Duguay, C., Essery, R., Haas, C., Hélière, F., Kern, M., Macelloni, G., Malnes, E., Nagler, T., Pulliainen, J., Rebhan, H., and Thompson, A.: Cold Regions Hydrology High-Resolution Observatory for Snow and Cold Land Processes, Proc. IEEE, 98, 752–765, https://doi.org/10.1109/JPROC.2009.2038947, 2010.

Royer, A., Roy, A., Montpetit, B., Saint-Jean-Rondeau, O., Picard, G., Brucker, L., and Langlois, A.: Comparison of commonly-used microwave radiative transfer models for snow remote sensing, Remote Sensing of Environment, 190, 247–259, https://doi.org/10.1016/j.rse.2016.12.020, 2017.

Sandells, M., Essery, R., Rutter, N., Wake, L., Leppänen, L., and Lemmetyinen, J.: Microstructure representation of snow in coupled snowpack and microwave emission models, The Cryosphere, 11, 229–246, https://doi.org/10.5194/tc-11-229-2017, 2017.

Sandells, M., Rutter, N., Wivell, K., Essery, R., Fox, S., Harlow, C., Picard, G., Roy, A., Royer, A., and Toose, P.: Simulation of Arctic snow microwave emission in surface-sensitive atmosphere channels, The Cryosphere, 18, 3971–3990, https://doi.org/10.5194/tc-18-3971-2024, 2024.

Stroeve, J., Willatt, R., Downie, M., Saha, M., Nab, C., Fallows, A., Soriot, C., Mallett, R., Komarov, A., Nandan, V., Newman, T., Lukovich, J., and Yackel, J.: Mapping snow on northern winter roads: a dual-frequency polarimetric radar approach for snow characterization over land, lake and sea ice, The Cryosphere, 20, 4367–4399, https://doi.org/10.5194/tc-20-4367-2026, 2026.

Sturm, M. and Holmgren, J.: An Automatic Snow Depth Probe for Field Validation Campaigns, Water Resources Research, 54, 9695–9701, https://doi.org/10.1029/2018WR023559, 2018.

Sturm, M. and Liston, G. E.: The snow cover on lakes of the Arctic Coastal Plain of Alaska, U.S.A., J. Glaciol., 49, 370–380, https://doi.org/10.3189/172756503781830539, 2003.

Sturm, M. and Liston, G. E.: Revisiting the Global Seasonal Snow Classification: An Updated Dataset for Earth System Applications, Journal of Hydrometeorology, https://doi.org/10.1175/JHM-D-21-0070.1, 2021.

SWOT: SWOT Level 2 Water Mask Raster Image Data Product, https://doi.org/10.5067/SWOT-RASTER-D, 2025.

© Author(s) 2026. CC BY 4.0 License.

Taelman, C., Landy, J., Mallett, R., and Itkin, P.: Empirical evidence of overestimated Ku-band sea ice radar freeboards in satellite altimetry, EGUsphere [preprint], https://doi.org/10.5194/egusphere-2026-1662, 2026.

Thompson, A. and Kelly, R.: Considerations for Ku-Band Radar Retrieval of Snow Water Equivalent at Mid-Latitude Ontario Agricultural Sites, Canadian Journal of Remote Sensing, 47, 119–142, https://doi.org/10.1080/07038992.2021.1898938, 2021a.

Thompson, A. and Kelly, R.: Estimating wind slab thickness in a Tundra snowpack using Ku-band scatterometer observations, Remote Sensing Letters, 12, 1123–1135, https://doi.org/10.1080/2150704X.2021.1961174, 2021b.

Thompson, A., Kelly, R., and King, J.: Sensitivity of Ku- and X-Band Radar Observations to Seasonal Snow in Ontario, Canada, Canadian Journal of Remote Sensing, 45, 829–846, https://doi.org/10.1080/07038992.2019.1704621, 2019.

Trudel, M., Gribi, T., Siles, G., Biancamaria, S., and Fjørtoft, R.: Impact of Ice, Snow, Wind, and Rain on Swot Water Detection over Canadian Lakes During Cal/Val, in: IGARSS 2024 - 2024 IEEE International Geoscience and Remote Sensing Symposium, IGARSS 2024 - 2024 IEEE International Geoscience and Remote Sensing Symposium, 3180–3183, https://doi.org/10.1109/IGARSS53475.2024.10641139, 2024.

Tsang, L. and Kong, J. A.: Scattering of Electromagnetic Waves: Advanced Topics, 1st ed., Wiley, https://doi.org/10.1002/0471224278, 2001.

Tsang, L., Kong, J. A., and Shin, R. T.: Theory of microwave remote sensing, in: Theory of microwave remote sensing by Tsang, 58641, 1985.

Tsang, L., Durand, M., Derksen, C., Barros, A. P., Kang, D.-H., Lievens, H., Marshall, H.-P., Zhu, J., Johnson, J., King, J., Lemmetyinen, J., Sandells, M., Rutter, N., Siqueira, P., Nolin, A., Osmanoglu, B., Vuyovich, C., Kim, E., Taylor, D., Merkouriadi, I., Brucker, L., Navari, M., Dumont, M., Kelly, R., Kim, R. S., Liao, T.-H., Borah, F., and Xu, X.: Review article: Global monitoring of snow water equivalent using high-frequency radar remote sensing, The Cryosphere, 16, 3531–3573, https://doi.org/10.5194/tc-16-3531-2022, 2022.

Ulaby, F. T. and Herschel Stiles, W.: Microwave response of snow, Advances in Space Research, 1, 131–149, https://doi.org/10.1016/0273-1177(81)90389-6, 1981.

Ulaby, F. T. and Long, D. G.: Surface-scattering models and land observations, in: *Microwave Radar and Radiometric Remote Sensing*, University of Michigan Press, Ann Arbor, USA, 421–460, ISBN 978-0-472-11935-6, 2014

https://doi.org/10.5194/egusphere-2026-5457
Preprint. Discussion started: 2 November 2026
© Author(s) 2026. CC BY 4.0 License.

Vargel, C., Royer, A., St-Jean-Rondeau, O., Picard, G., Roy, A., Sasseville, V., and Langlois, A.: Arctic and subarctic snow microstructure analysis for microwave brightness temperature simulations, Remote Sensing of Environment, 242, 111754, https://doi.org/10.1016/j.rse.2020.111754, 2020.

Veijola, K., Cohen, J., Mäkynen, M., Lemmetyinen, J., Praks, J., and Cheng, B.: X- and Ku-Band SAR Backscattering Signatures of Snow-Covered Lake Ice and Sea Ice, Remote Sensing, 16, 369, https://doi.org/10.3390/rs16020369, 2024.

Wakabayashi, H., Nishio, F., and Jeffries, M.: C-band backscattering characteristics of lake ice in Northern Alaska during spring thaw period, *J. Remote Sens. Soc. Jpn.*, 19, 333–341, https://doi.org/10.11440/rssj1981.19.333, 1999.

Wang, Z., Zhang, H., Xu, L., Guo, Z., Qiu, Y., and Li, X.: Forward simulation of thin ice backscatter mechanism in the Bohai Sea region based on the MSIB and SMRT coupling model, International Journal of Digital Earth, 18, 2515538, https://doi.org/10.1080/17538947.2025.2515538, 2025.

Welch, J. J. and Kelly, R. E. J.: A prototype passive microwave retrieval algorithm for tundra snow density, The Cryosphere, 19, 5259–5282, https://doi.org/10.5194/tc-19-5259-2025, 2025.

Woolley, G. J., Rutter, N., Wake, L., Vionnet, V., Derksen, C., Meloche, J., Montpetit, B., Leroux, N. R., Essery, R., Hould Gosselin, G., and Marsh, P.: Simulating snow properties and Ku-band backscatter across the forest-tundra ecotone, The Cryosphere, 20, 1315–1338, https://doi.org/10.5194/tc-20-1315-2026, 2026.

Yoon, S.: The Surface Water and Ocean Topography (SWOT) Mission for River and Lake Ice Application, M.S. thesis, Southern Methodist University, Dallas, TX, USA, https://scholar.smu.edu/hum_sci_earthsciences_etds/39, 2025.

Zakharova, E., Agafonova, S., Duguay, C., Frolova, N., and Kouraev, A.: River ice phenology and thickness from satellite altimetry: potential for ice bridge road operation and climate studies, The Cryosphere, 15, 5387–5407, https://doi.org/10.5194/tc-15-5387-2021, 2021.

Zhu, J., Tan, S., King, J., Derksen, C., Lemmetyinen, J., and Tsang, L.: Forward and Inverse Radar Modeling of Terrestrial Snow Using SnowSAR Data, IEEE Trans. Geosci. Remote Sensing, 56, 7122–7132, https://doi.org/10.1109/TGRS.2018.2848642, 2018.